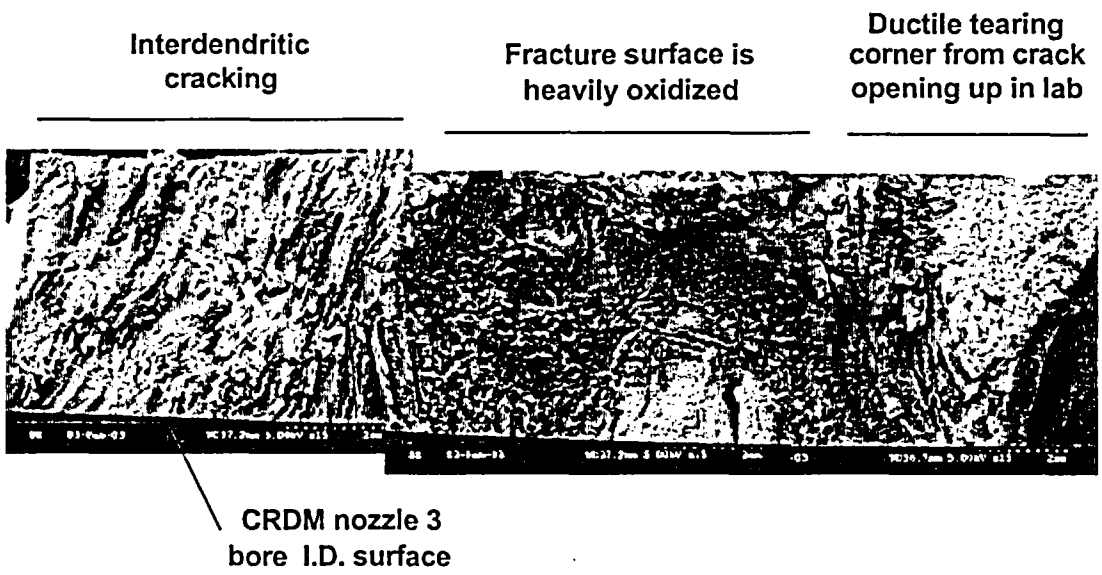

Figure 7.2.4.2: Low magnification SEM mosaic of the fracture surface after opening-up the axial crack. BSE 6.7X

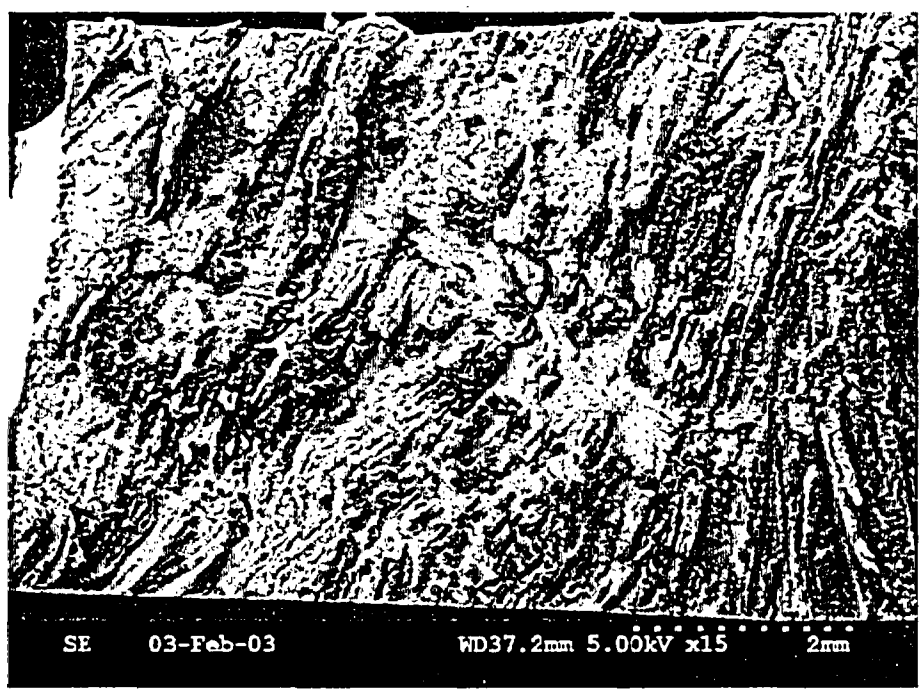

Figure 7.2.4.3: Higher magnification of the left section in Figure 7.2.4.2. Cracking is interdendritic exposing a well-defined columnar solidification structure.

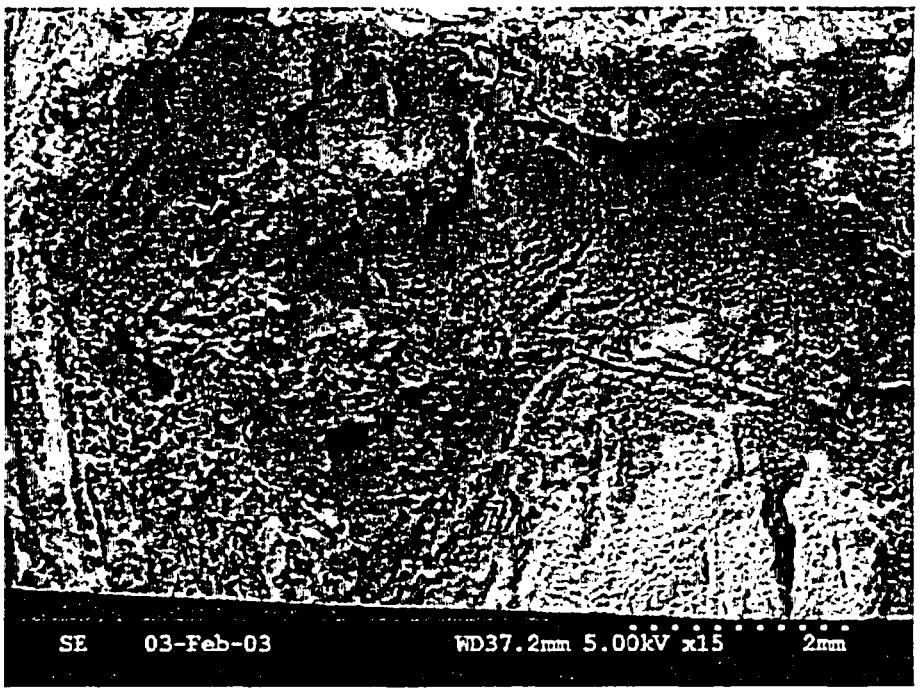

Figure 7.2.4.4: Higher magnification of the middle section in Figure 7.2.4.2. The fracture surface is heavily oxidized; the fracture mode is indeterminate.

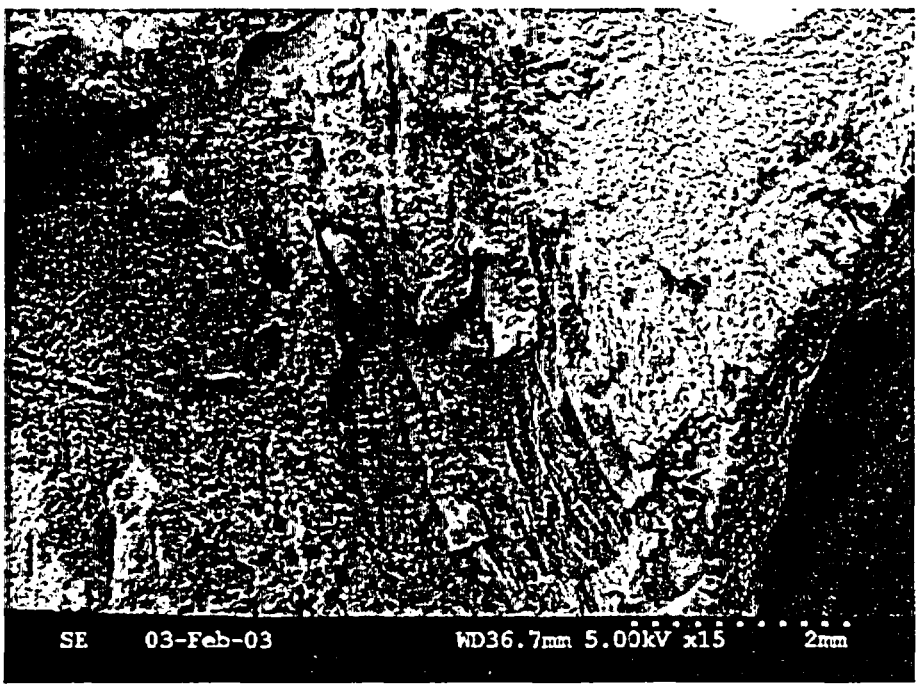

Figure 7.2.4.5: Higher magnification of the right section in Figure 7.2.4.2. Cracking to the left side of ductile tearing (lab fracture) is interdendritic.

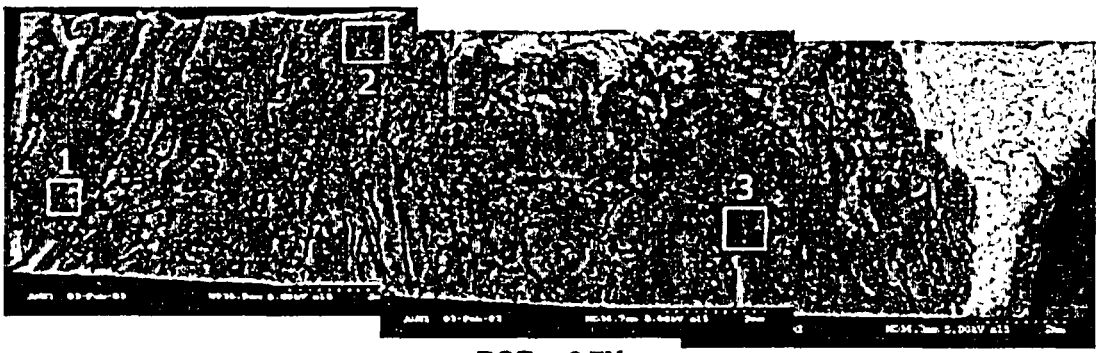

BSE 6.7X

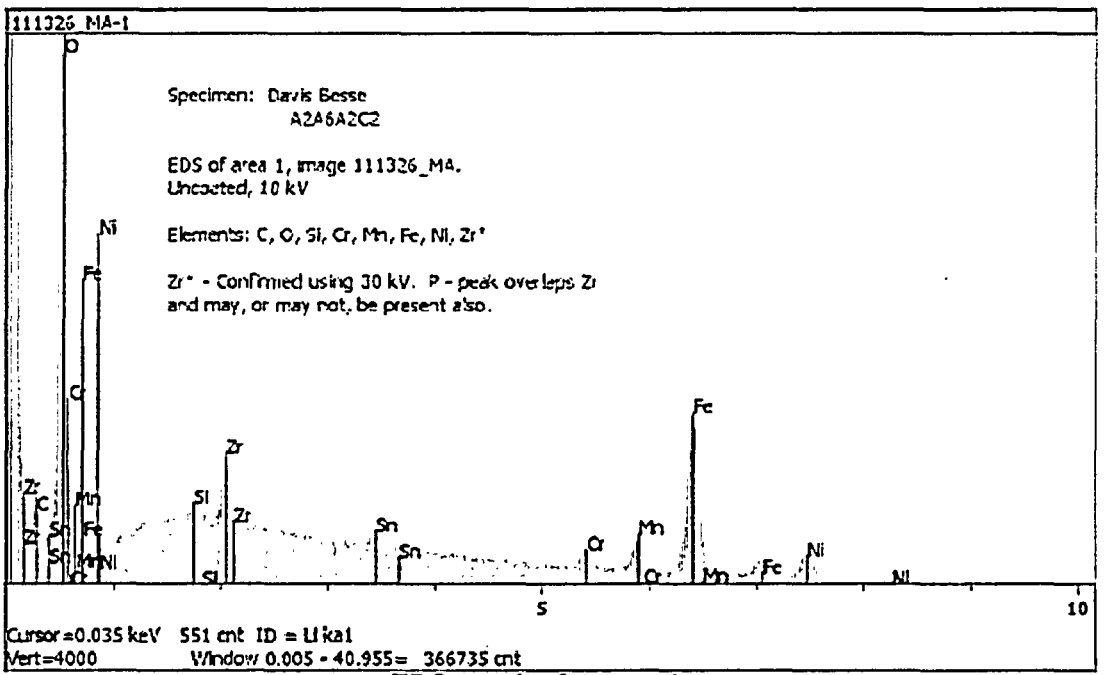

EDS results for area 1.

Figure 7.2.4.6: BSE micrograph mosaic of the open crack surface (same area as Figure 7.2.4.2) along with EDS results for three areas of the fracture surface. The dark area in the BSE image indicates the fracture surface was covered by a thick oxide layer. The light area (right side) indicates a fresh fracture surface due to crack opening-up (i.e., less oxide on surface). For area 1, the primary elements included carbon, oxygen, silicon, chromium, manganese, iron, nickel, and zirconium.

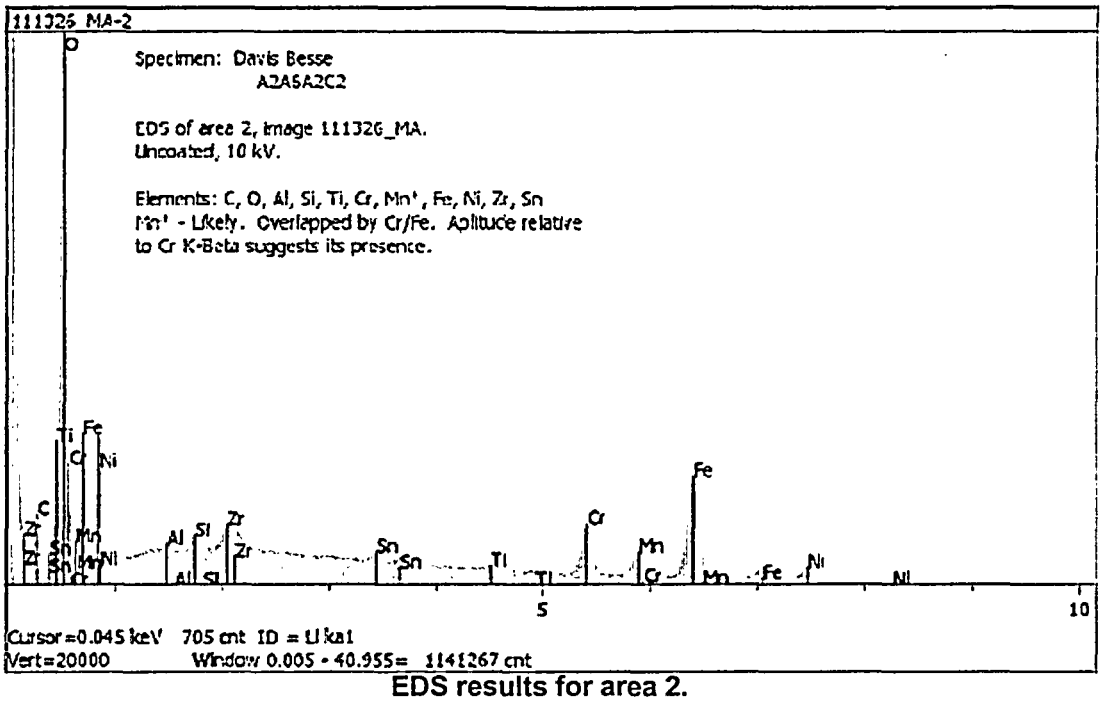

EDS results for area 2.

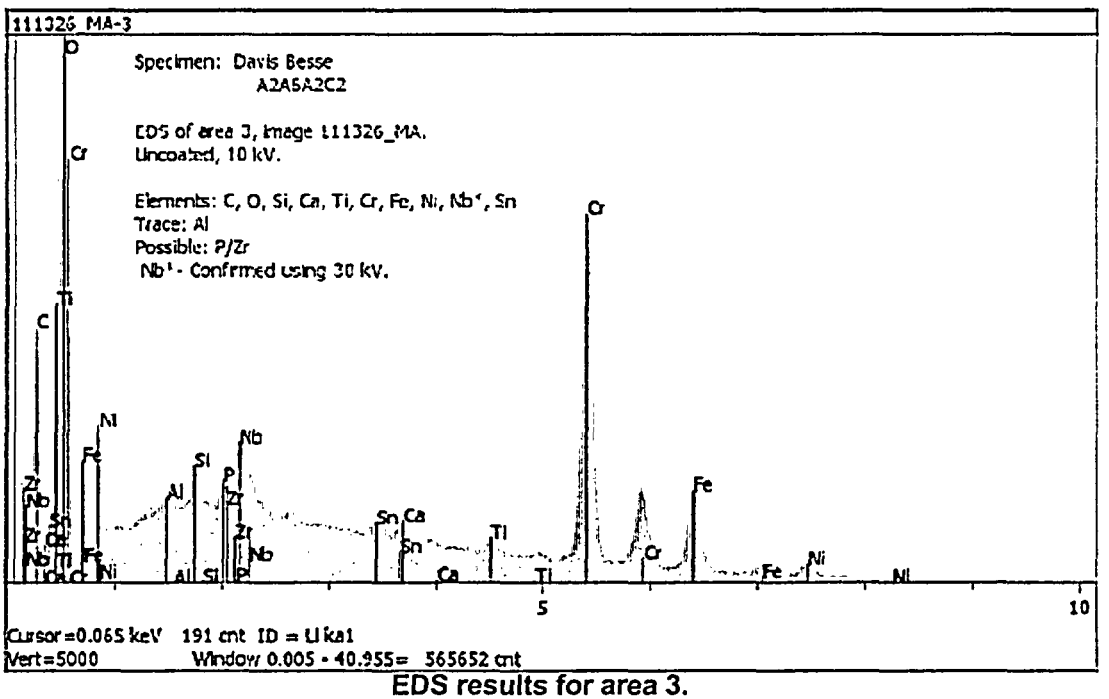

EDS results for area 3.

Figure 7.2.4.6 (cont.): For area 2, the primary elements included carbon, oxygen, silicon, chromium, manganese, iron, nickel, and zirconium. Similar results were obtained for area 3, except area 3 also contained niobium and calcium.

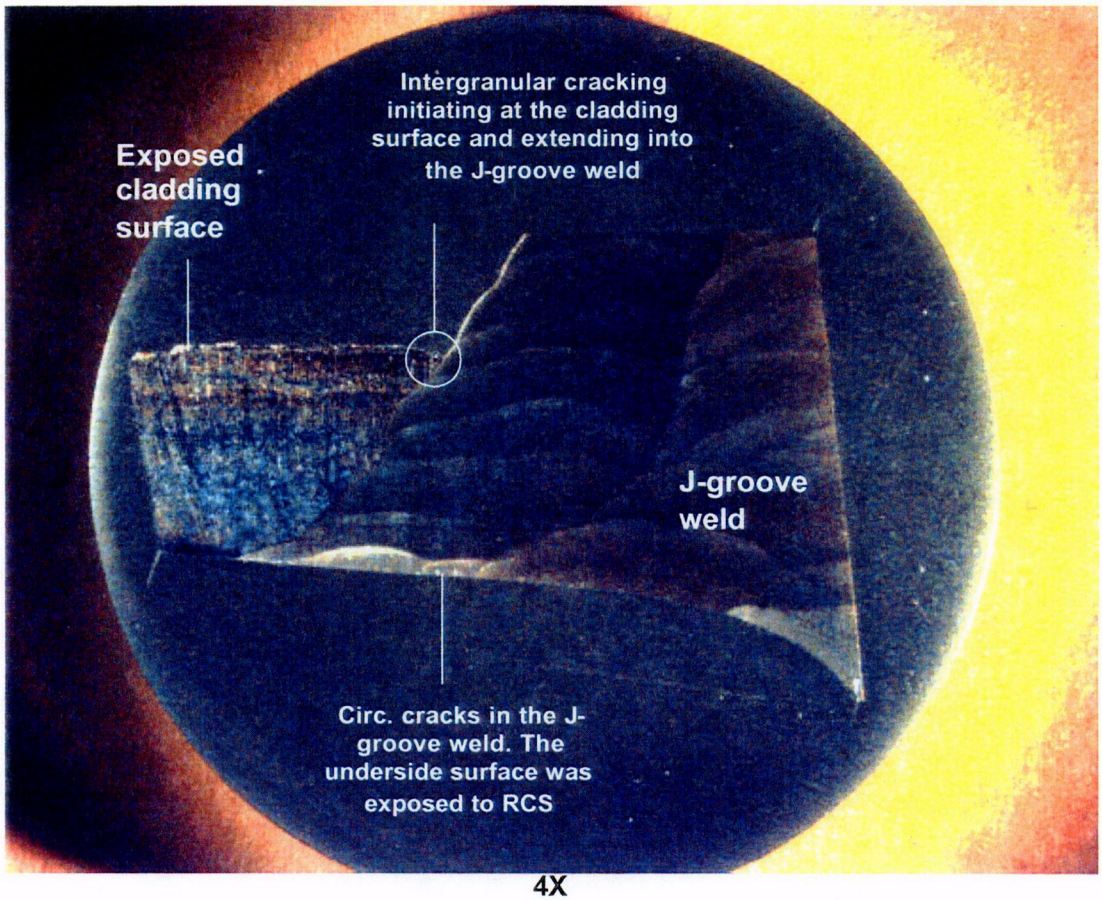

Figure 7.3.1.1: Macro photograph of metallographic sample A2A6A2B2. The mounted surface is through the J-groove weld at ~45°. Refer to Figures 5.6 and 5.7 for the sample orientation.

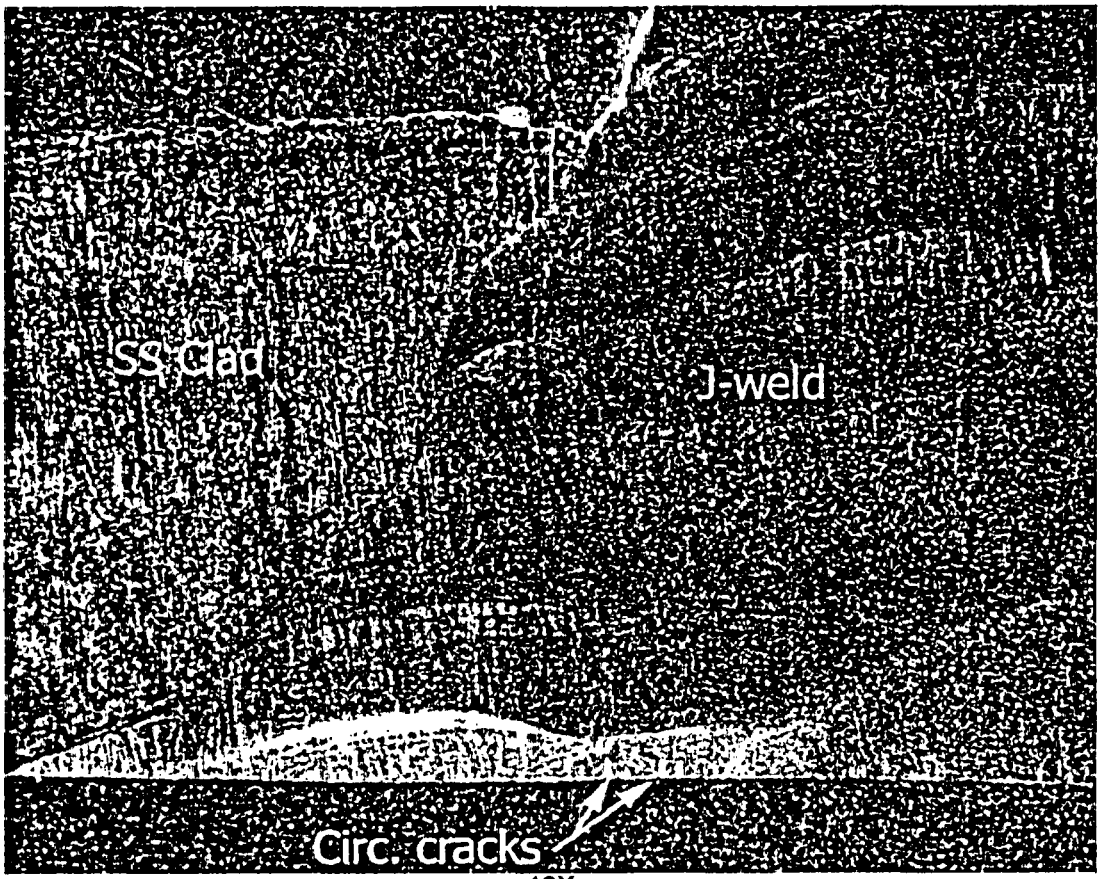

Figure 7.3.1.2: Slightly higher magnification photograph of metallographic mount A2A6A2B2.

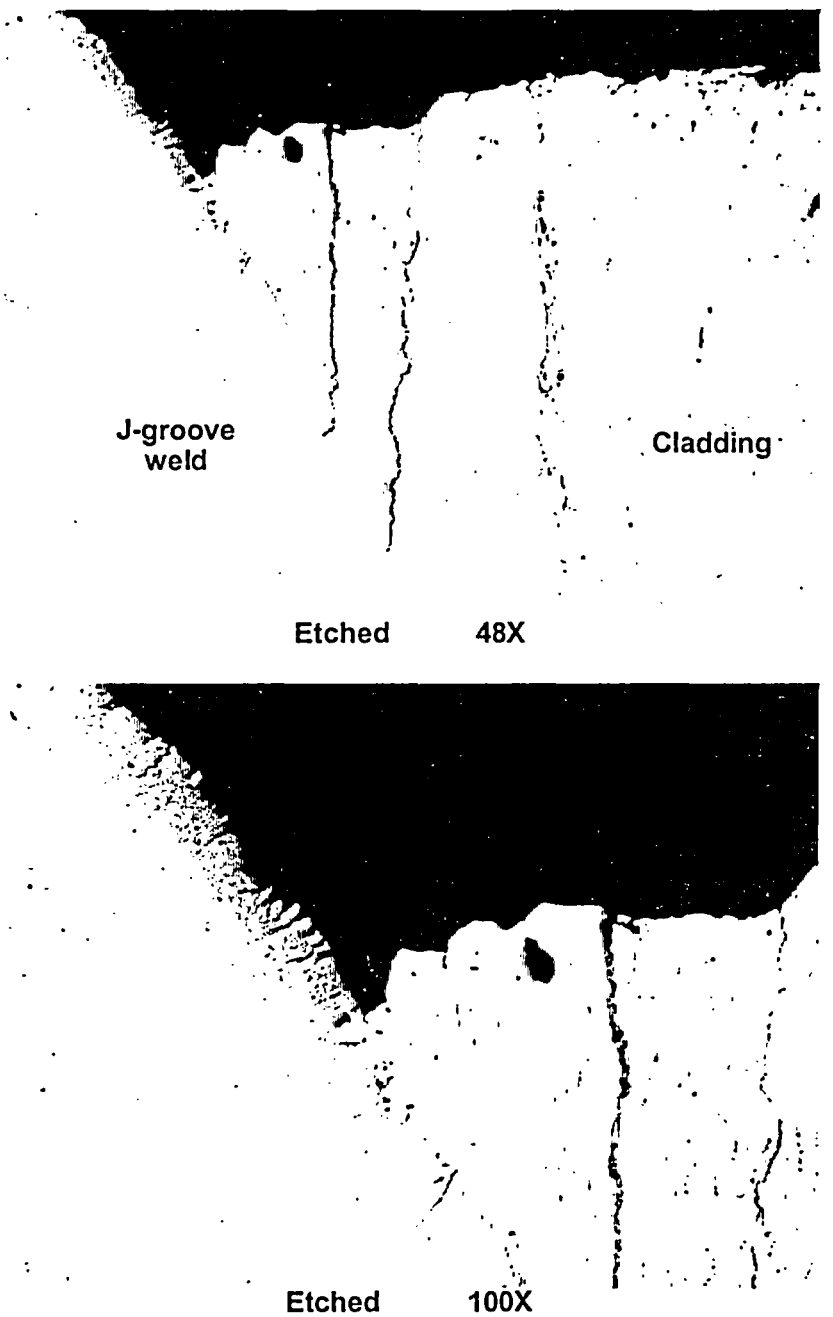

Figure 7.3.1.3: Intergranular or interdendritic cracking initiating at the cladding surface and extending into the J-groove weld. Note that the micrographs shown are mirror image of the photo in Figure 7.3.1.2. Intergranular attack (IGA) is also evident on the exposed surface of J-groove weld and cladding (surface exposed to oxygenated boric acid). This cracking is likely initiated by IGA.

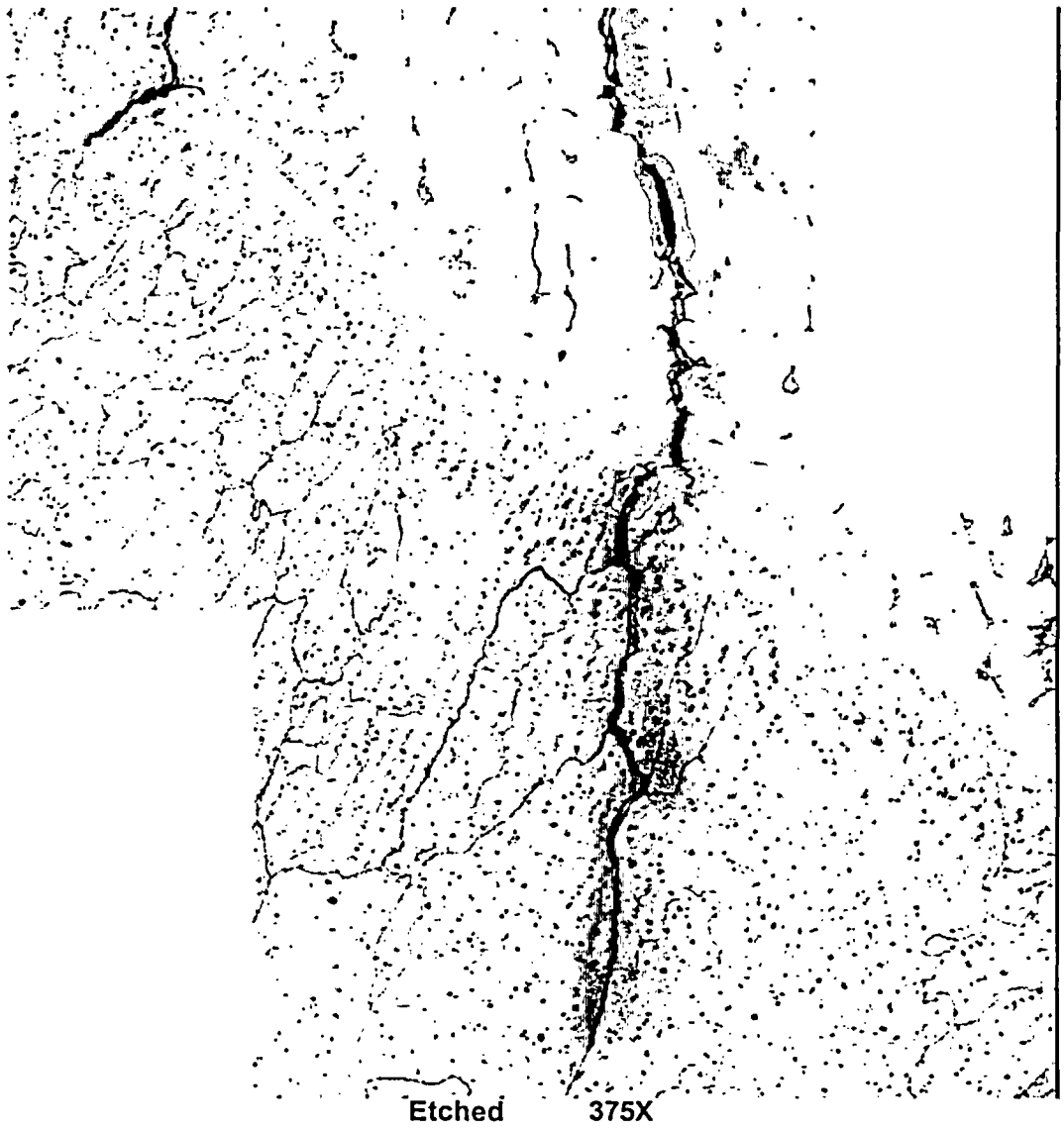

Figure 7.3.1.4: Higher magnification micrograph showing intergranular or interdendritic cracking initiating at the cladding surface and extending into the J-groove weld.

As-polished 48X

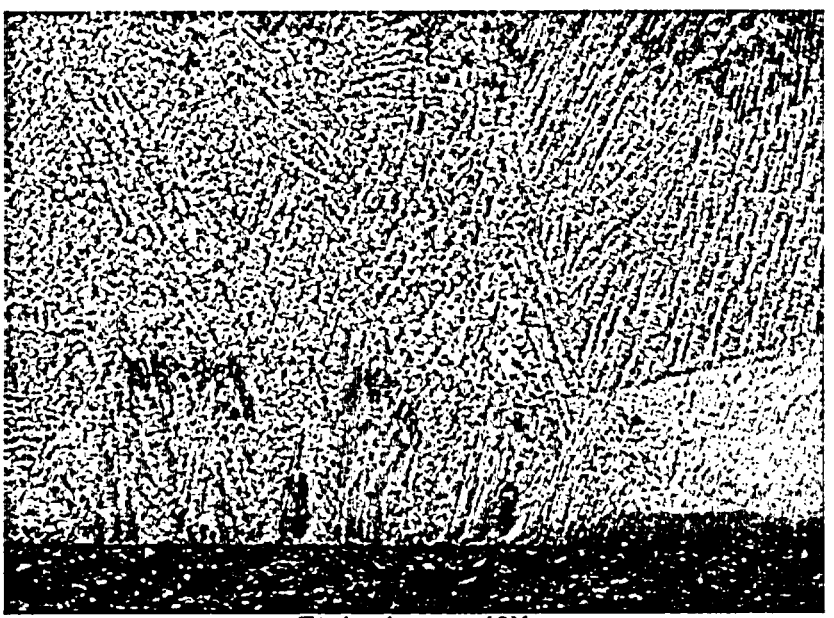

Etched 48X

Figure 7.3.1.5: Low magnification micrographs showing shallow circumferential cracking in the J-groove weld.

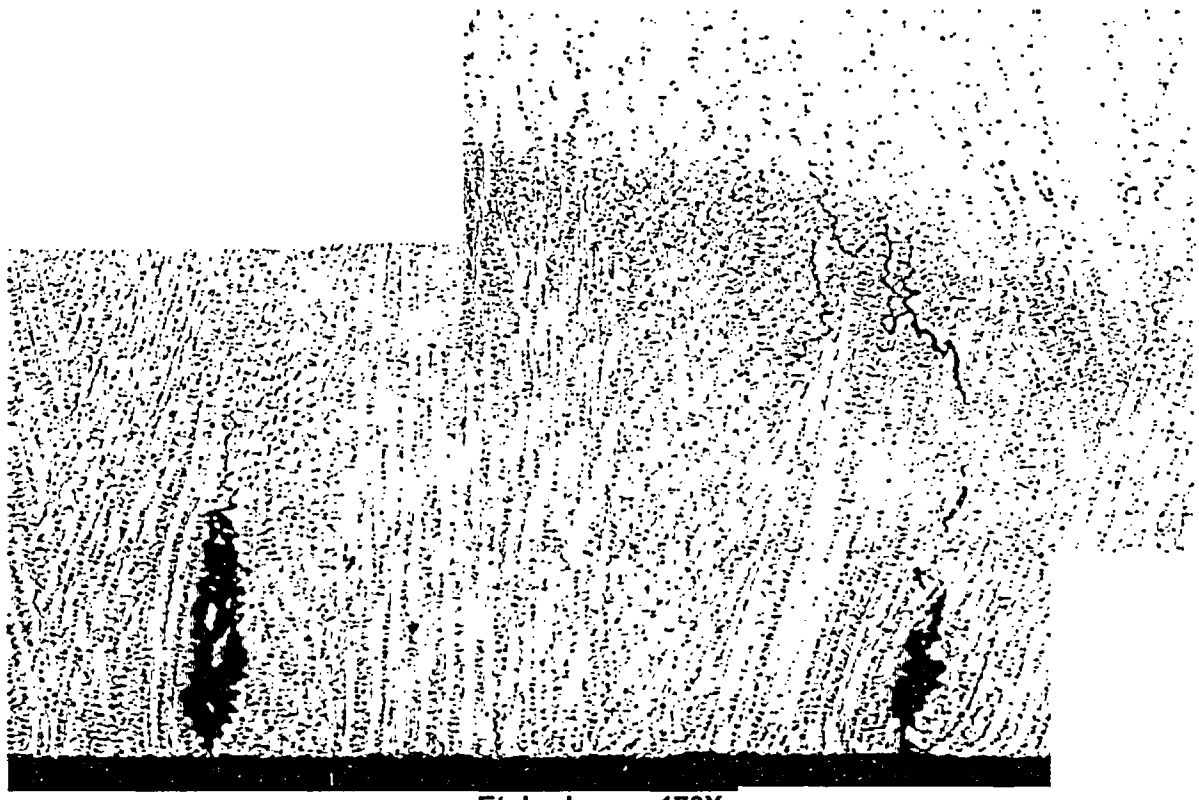

Figure 7.3.1.6: Micrograph showing the shallow circumferential cracks in the J-groove weld. The cracking is intergranular or interdendritic, with a maximum depth of approximately 0.019" below the surface. The two wider crack regions just below the surface may have been dendrites or grains encircled by cracks that subsequently dropped out during sample preparation.

Etched 190X

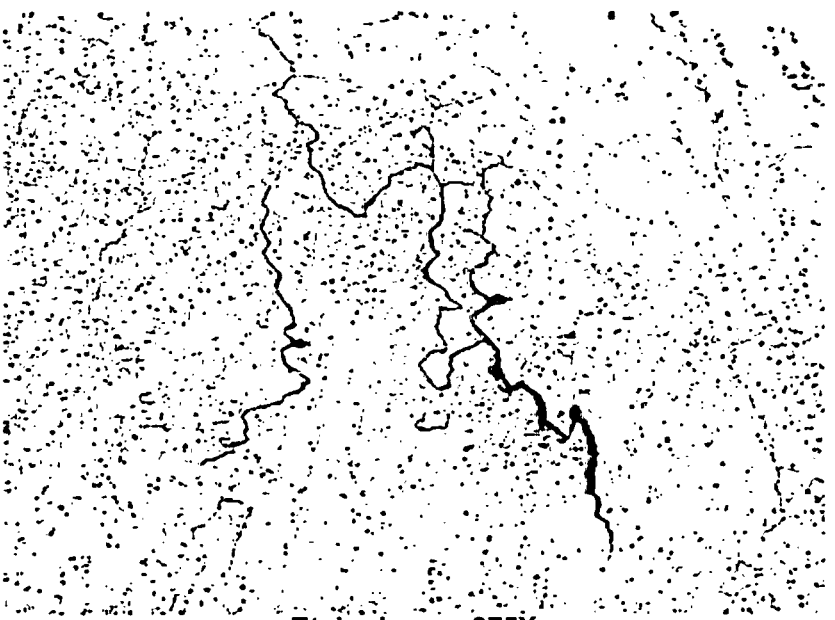

Etched 375X

Figure 7.3.1.7: Micrographs showing crack tips of the circumferential cracking in the J-groove weld.

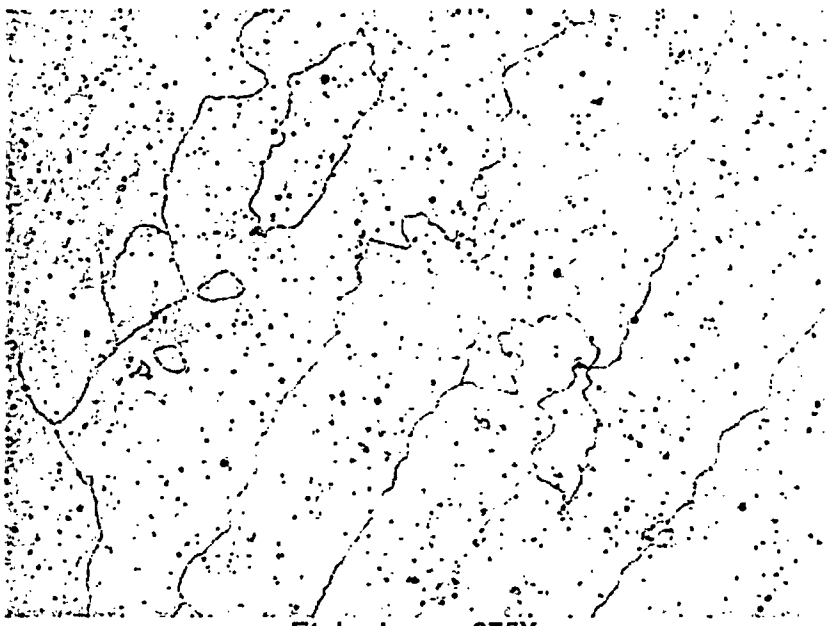

Figure 7.3.1.8: Typical J-groove weld microstructure.

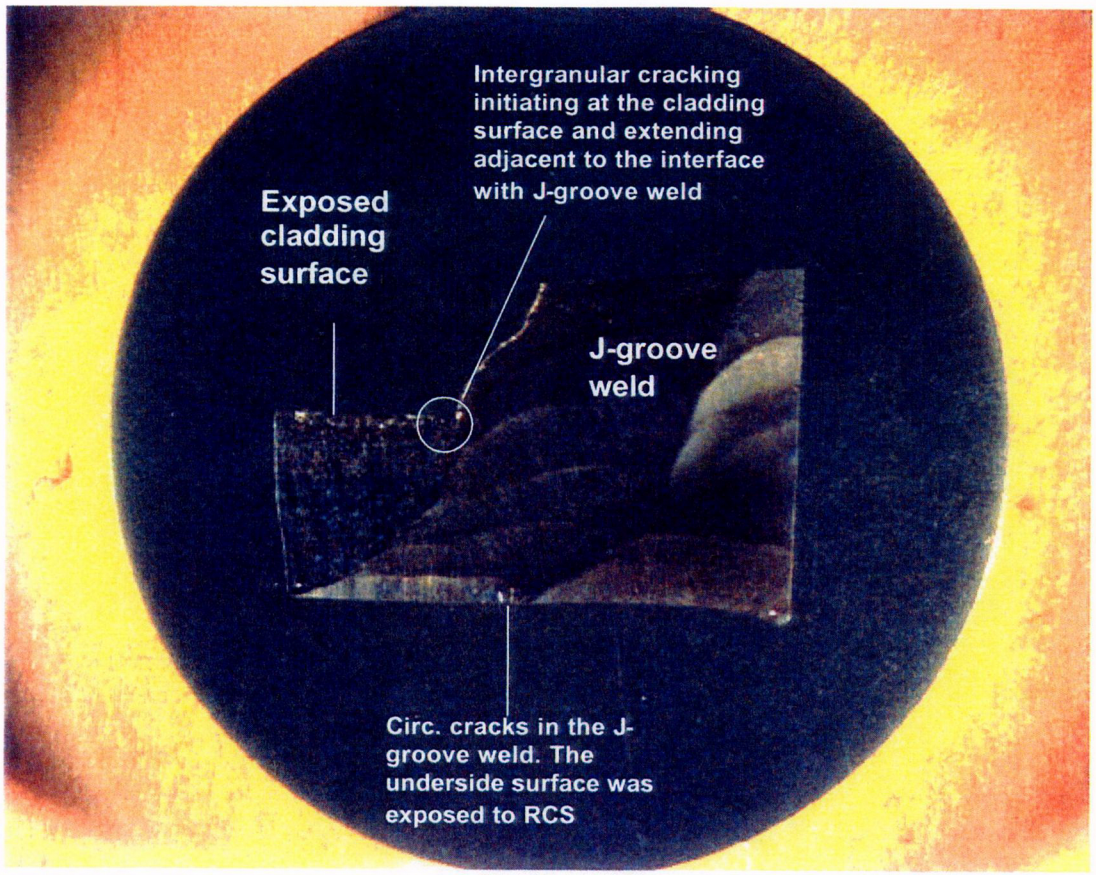

4X

Figure 7.3.2.1: Macro photograph of metallographic mount A2A6A2D2. The mounted surface is through the J-groove weld at ~30°. Refer to Figures 5.6 and 5.9 for the sample location.

Etched 100X

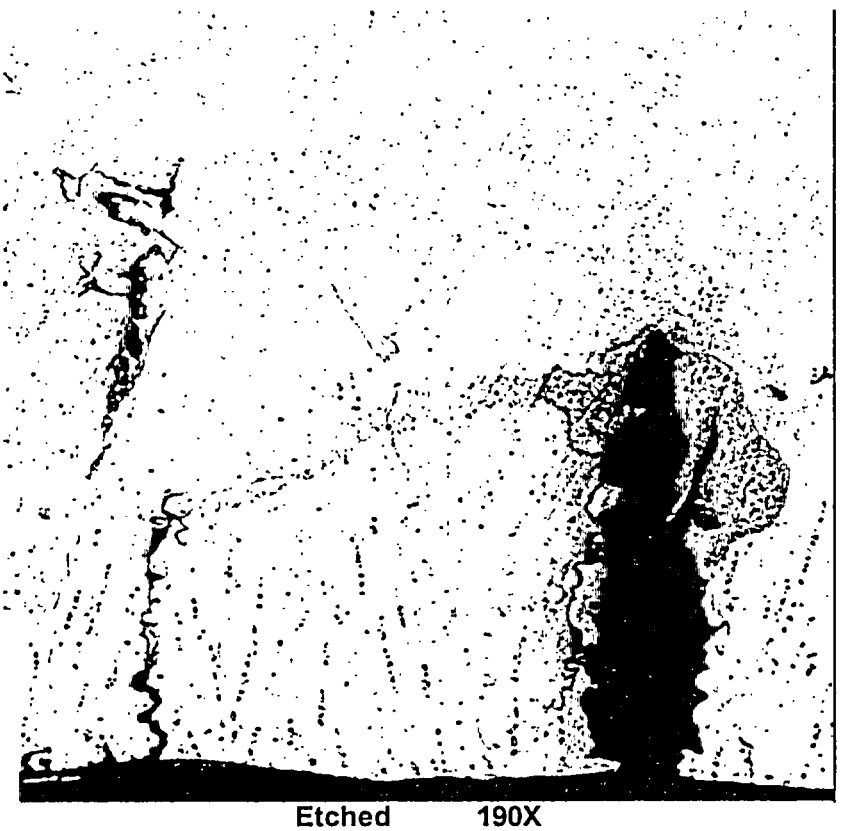

Etched 190X

Figure 7.3.2.2: Micrograph showing the circumferential intergranular/interdendritic cracks in the J-groove weld. The maximum cracking depth is approximately 0.018" below the surface. The cavity just below the surface may be due to dendrites or grains encircled by the cracks that dropped out during sample grinding and polishing.

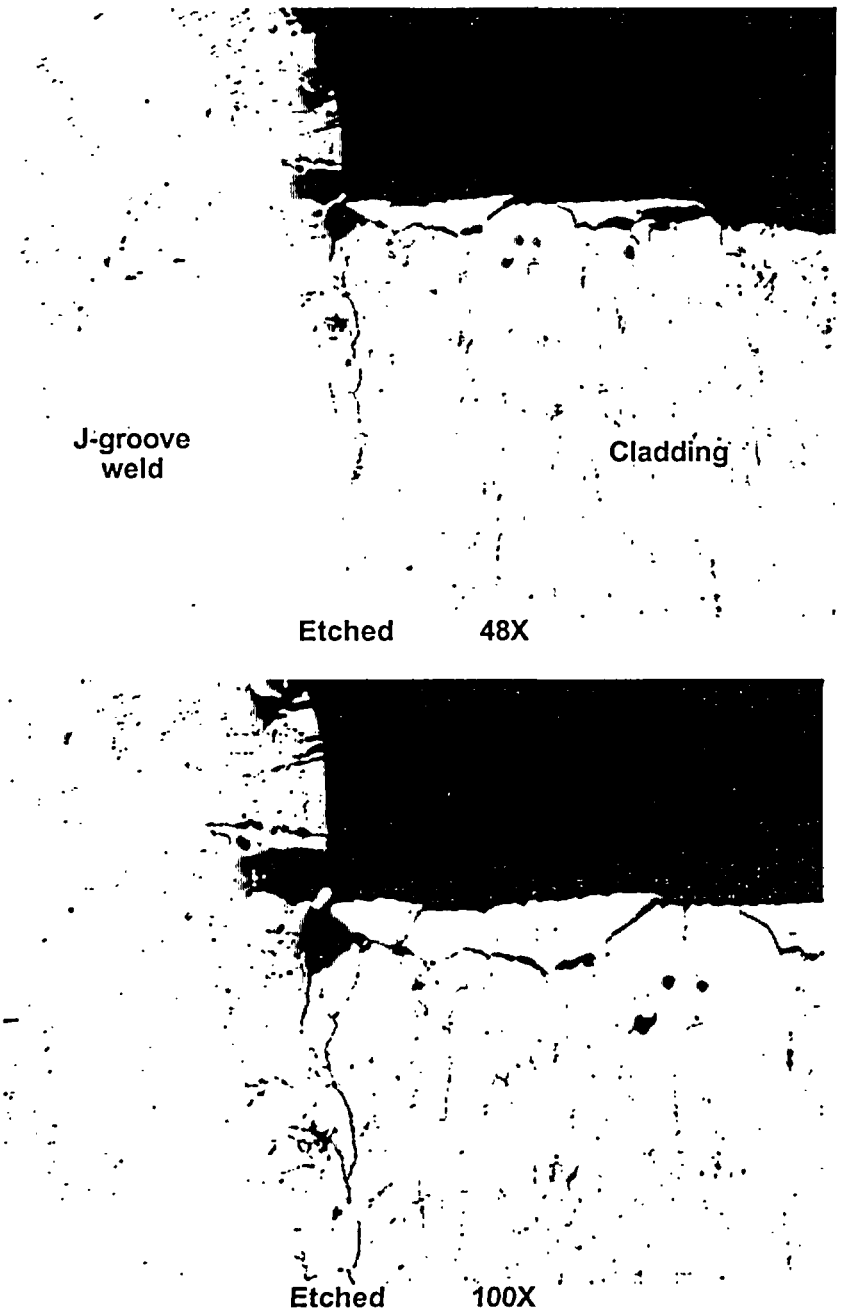

Figure 7.3.2.3: Micrographs showing the intergranular or interdendritic cracking between the J-groove weld and cladding interface. The micrographs shown here are mirror of the photo in Figure 7.3.2.1. Intergranular attack (IGA) is also evident on the exposed surface of J-groove weld and cladding (surface exposed to oxygenated boric acid). This cracking was likely initiated by IGA.

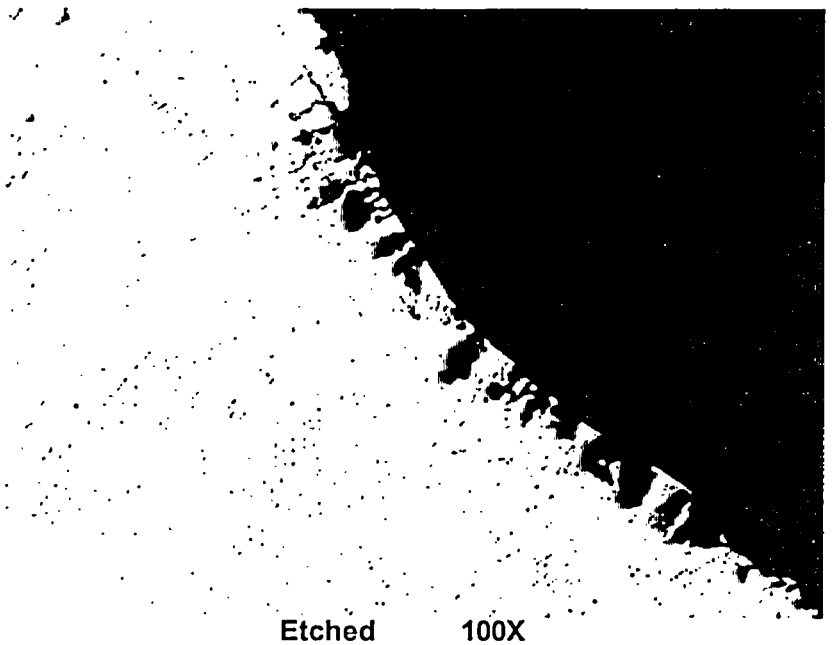

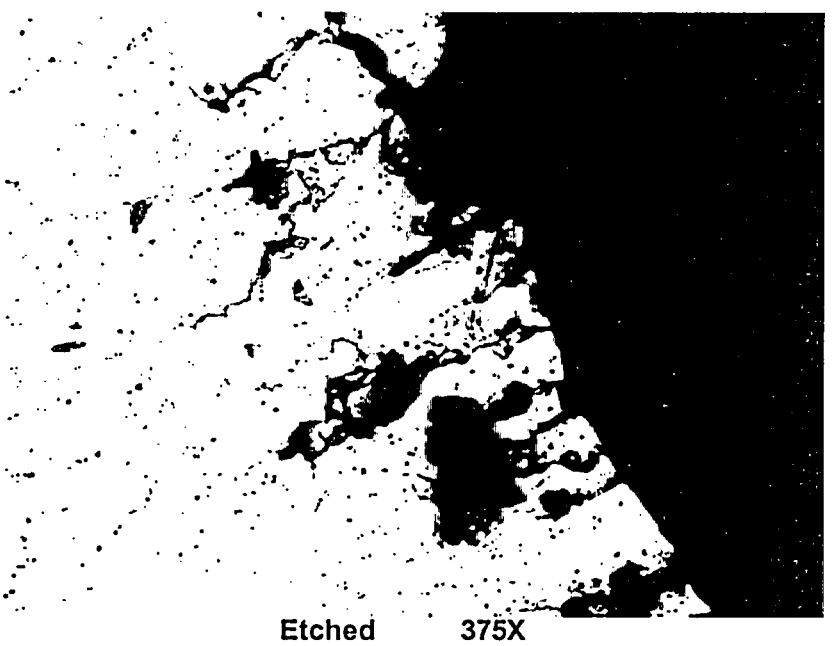

Figure 7.3.2.4: Intergranular attack (IGA) on the J-groove weld surface exposed to oxygenated boric acid.

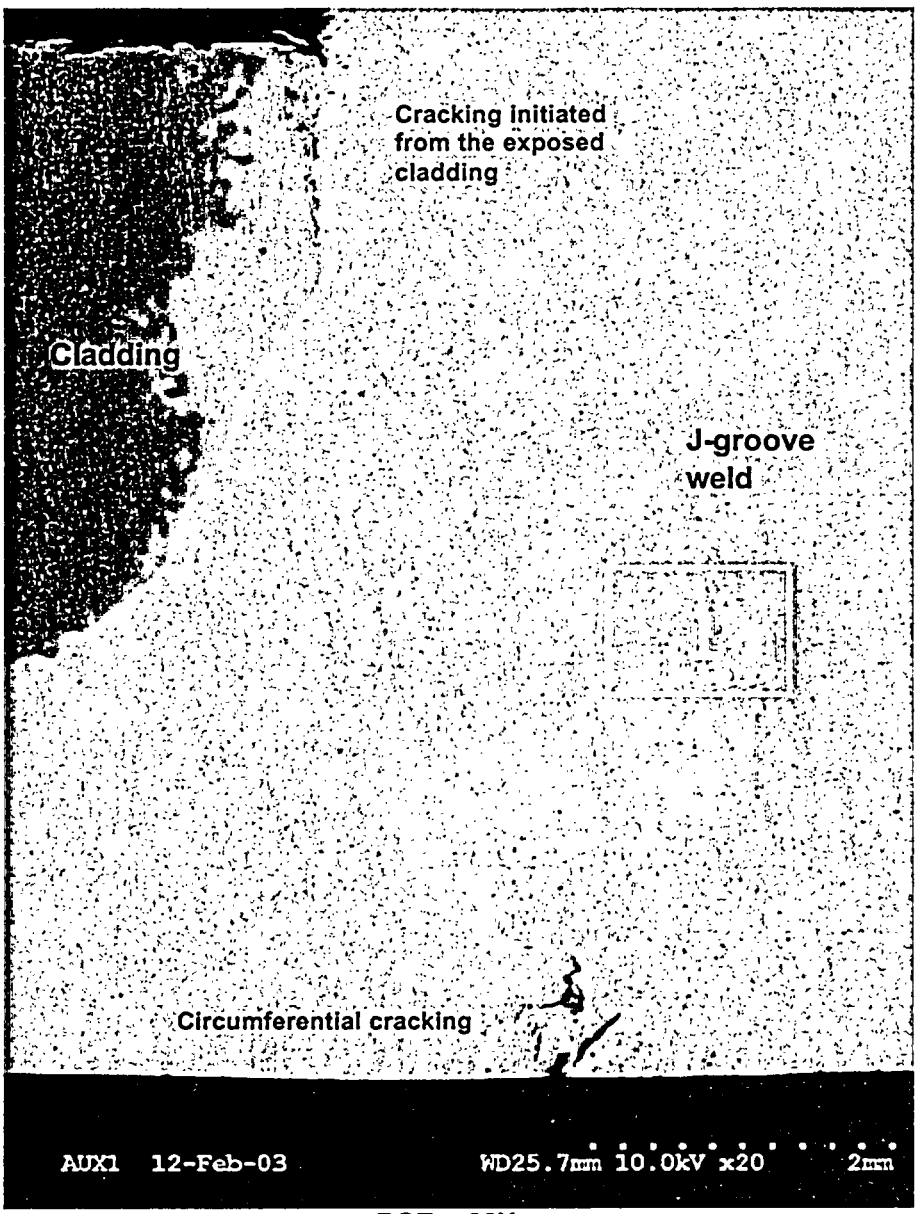

BSE 20X

Figure 7.3.3.1: Low magnification BSE micrograph of sample A2A6A2D2 showing the cracking in the exposed cladding surface and the axial cracking in the J-groove weld surface exposed to RCS. The EDS spectrum collected from area 1 is presented in Figure 7.3.3.2.

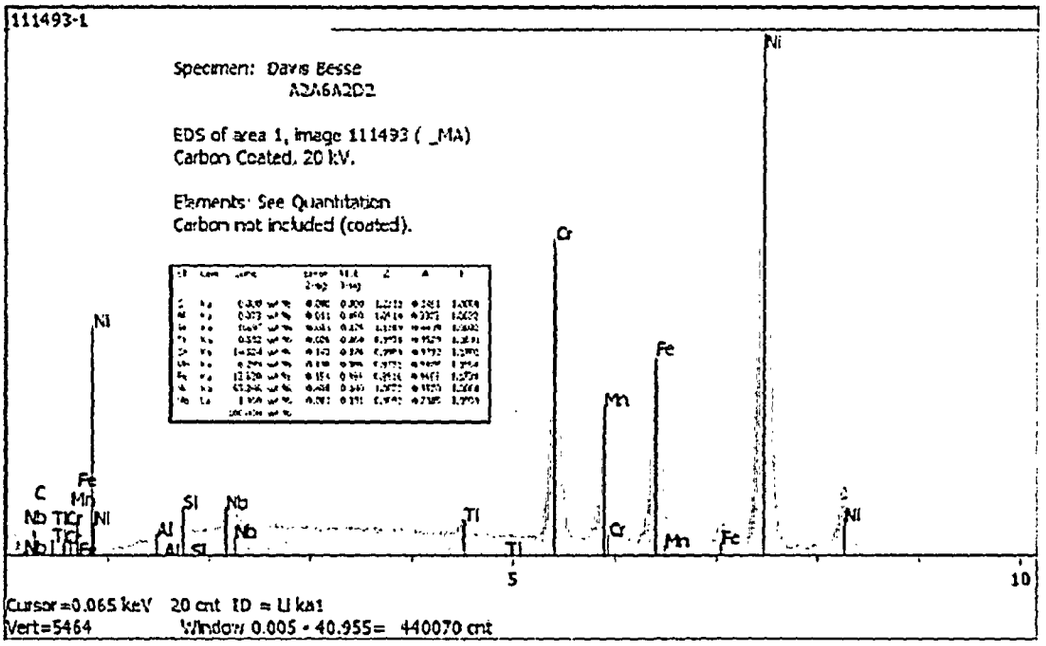

Figure 7.3.3.2: The EDS spectrum for area 1 in Figure 7.3.3.1. The semi-quantitative results from this area, which was located within the J-groove weld, were consistent with Alloy 182 weld metal.

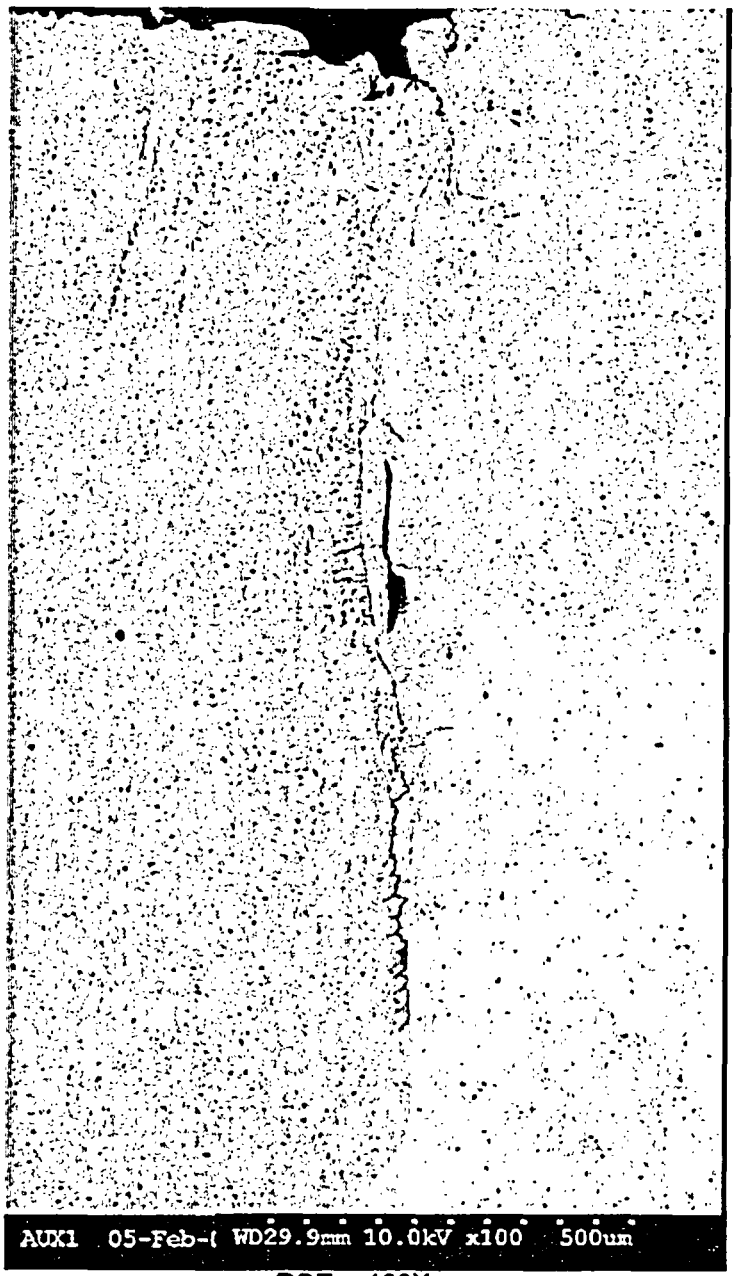

BSE 100X

Figure 7.3.3.3: Low magnification BSE micrograph showing the cracking that initiated from the exposed cladding surface (left side of figure). The maximum crack depth is approximately 0.055" below the cladding surface.

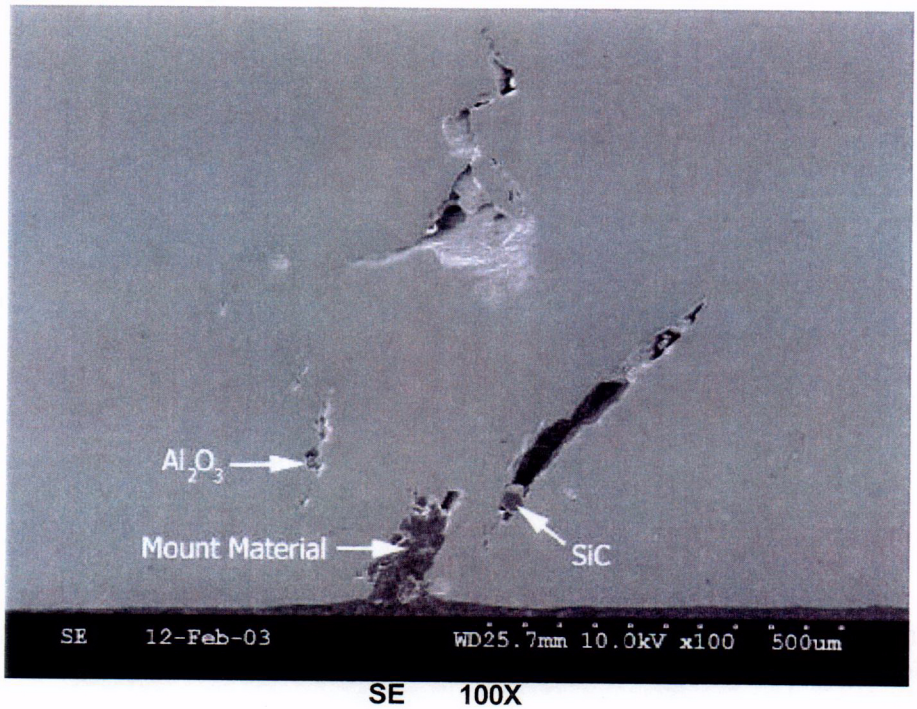

SE 100X

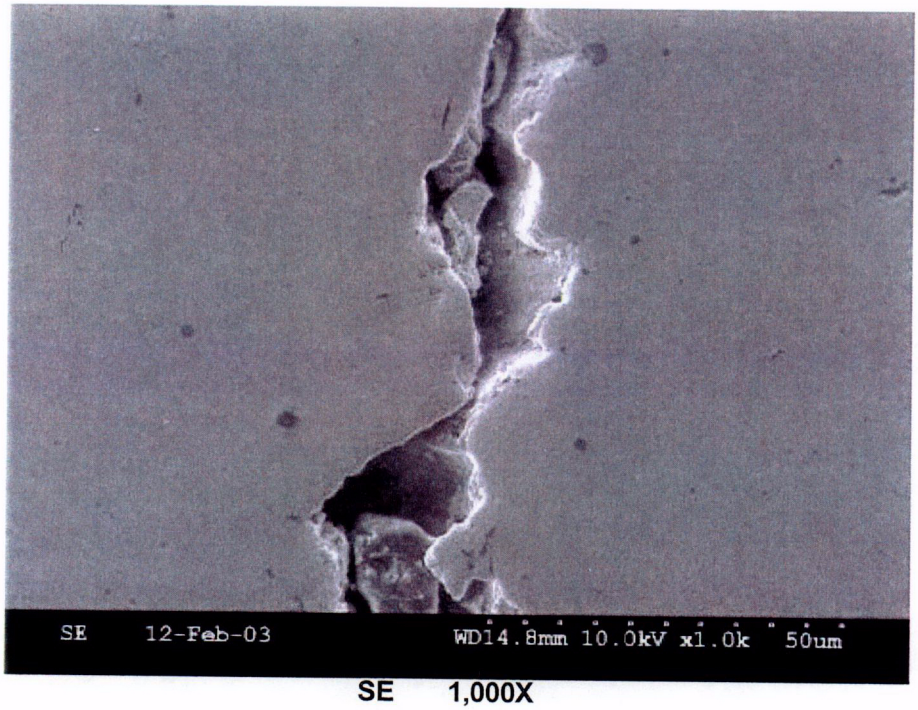

SE 1,000X

Figure 7.3.3.4: SE micrographs of the circumferential cracking in the J-groove weld. The maximum circumferential cracking depth is approximately 0.032" below the surface. Cracking was interdendritic in nature.

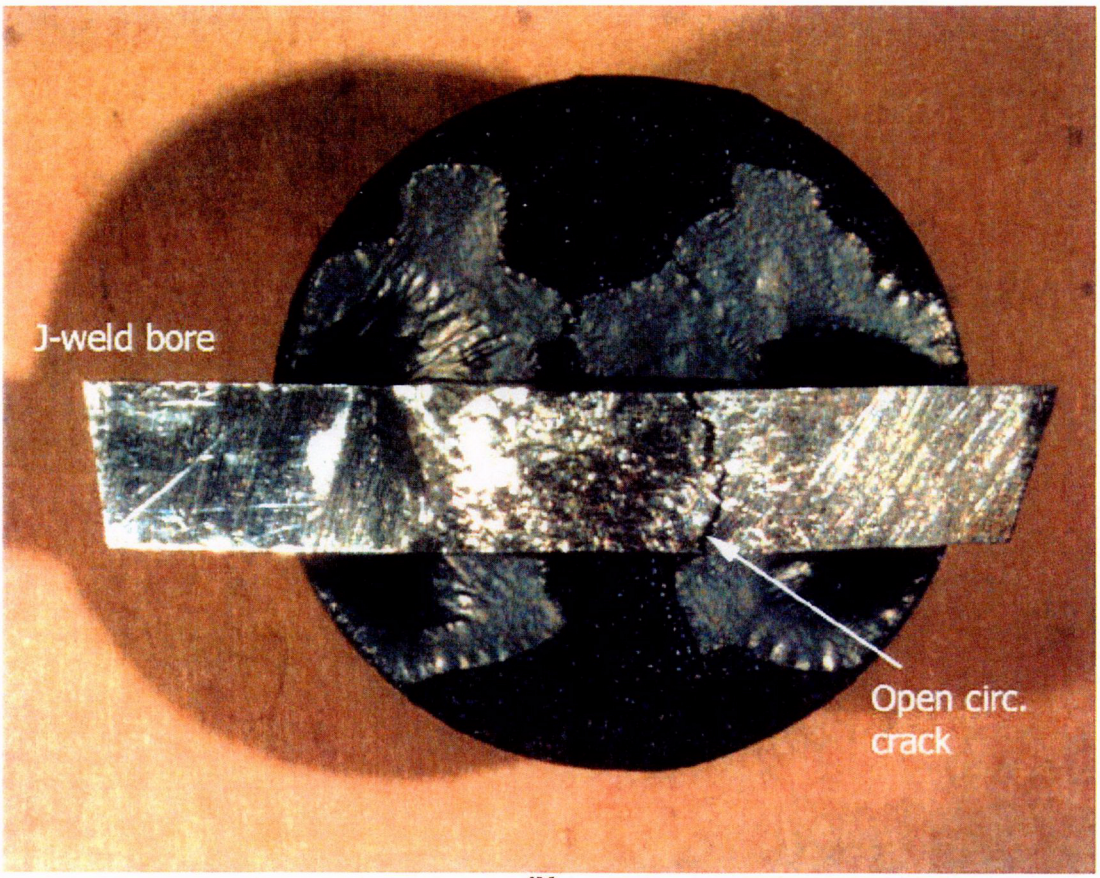

4X

Figure 7.3.4.1: Macro photograph of the opened-up circumferential cracking in the J-groove weld at ~30°. The underside surface of the J-groove weld (in contact with RCS) is shown. Refer to Figures 5.6 and 5.8 for the sample location. The rectangular sample (A2A6A2C2) is secured to the round SEM stub with black carbon tape.

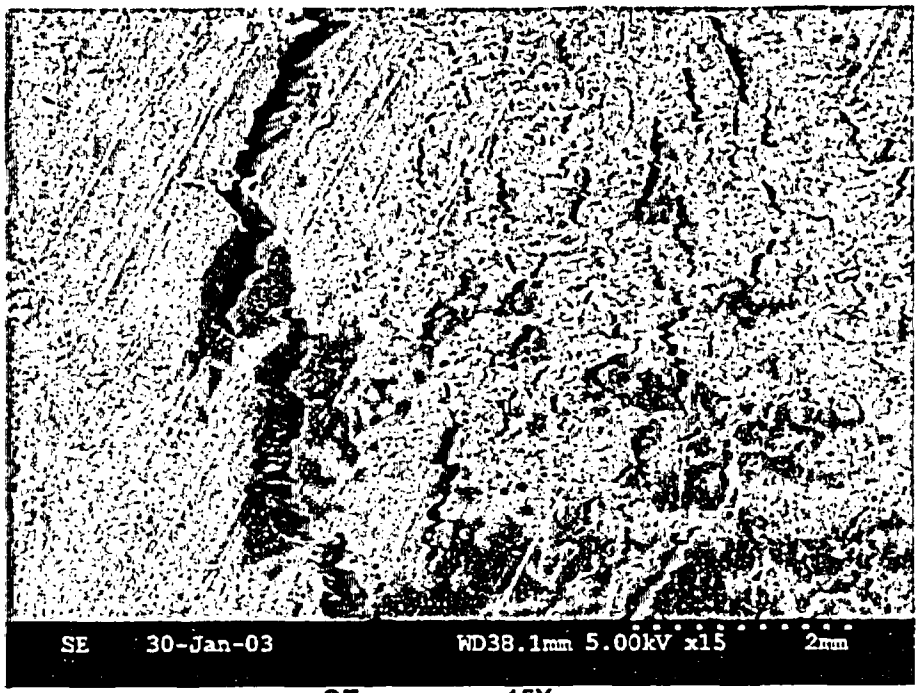

SE 15X

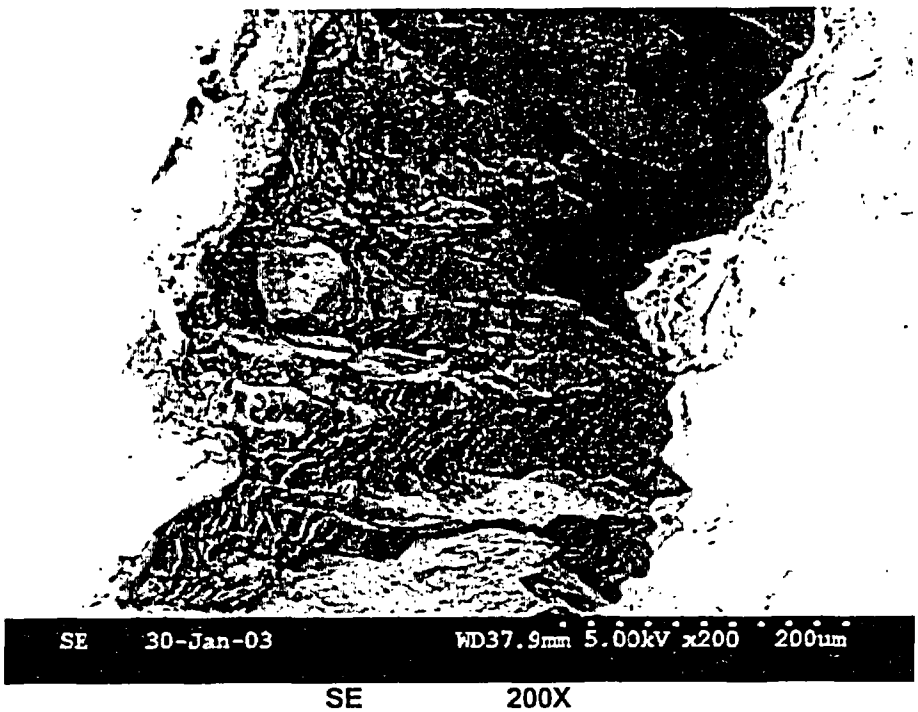

SE 200X

Figure 7.3.4.2: SE micrographs showing the shallow circumferential cracking in the J-groove weld. Cracking was interdendritic.

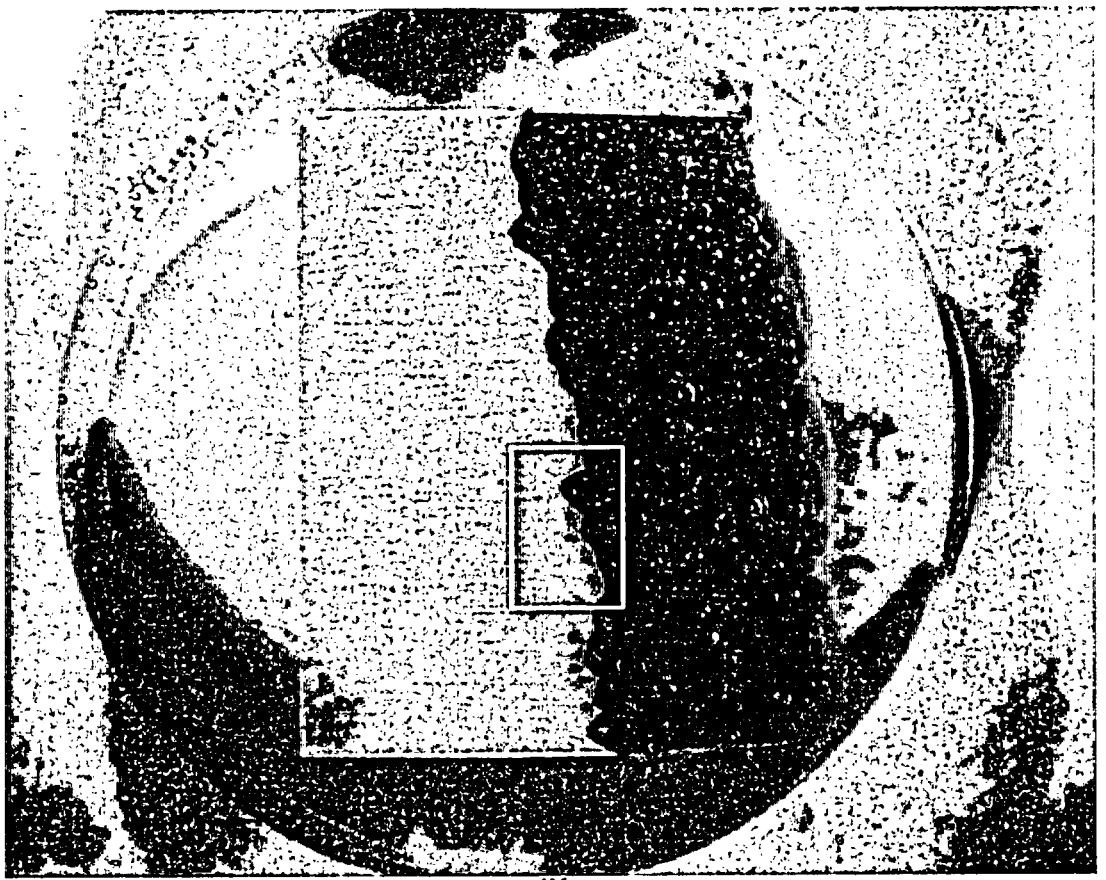

4X

Figure 8.1.1.1: Macro photograph of sample A1B2. Refer to Figures 5.13 and 5.14 for the sample location. The white box shows area enlarged in Figure 8.1.1.2.

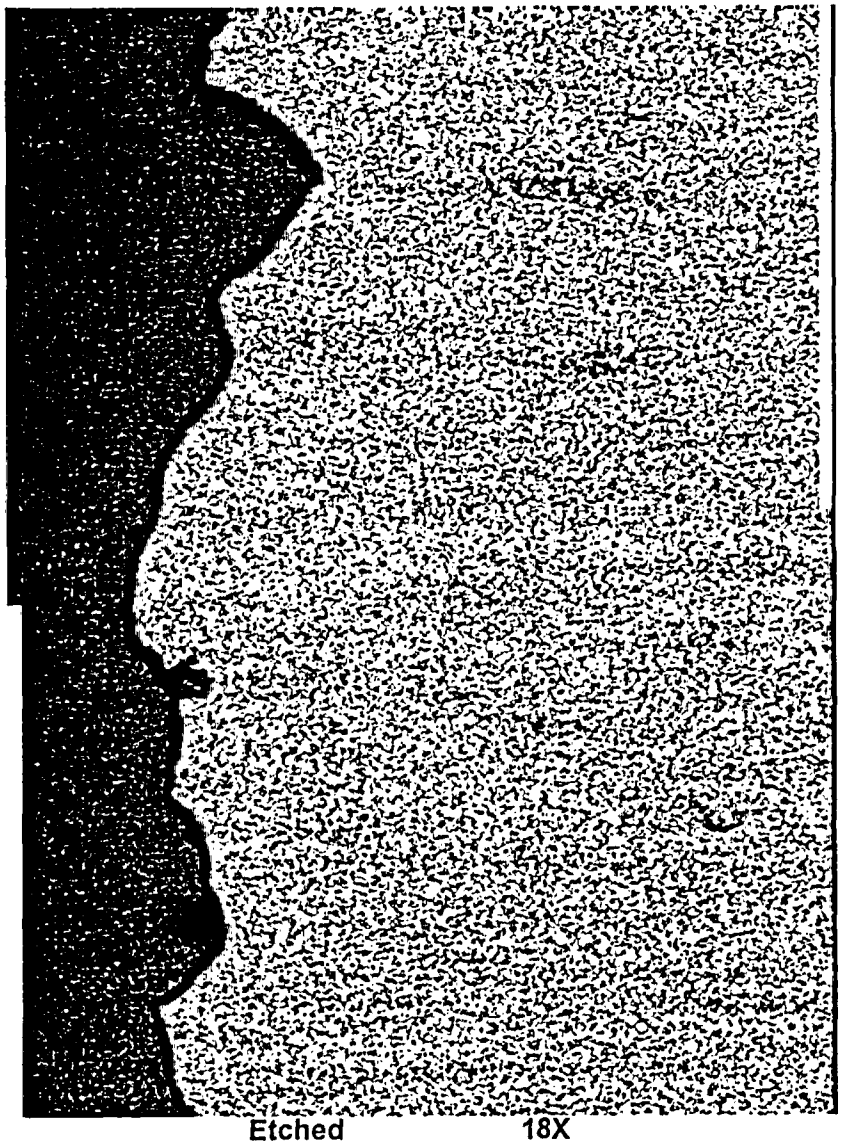

Figure 8.1.1.2: Low magnification micrograph showing horizontal striations aligned with the major axis of the RV head low alloy steel plate (SA-533, Gr. B (mod), Cl. 1). The striations are due to the segregation of carbides, which promote a slightly faster local corrosion rate along the striations. Note that this micrograph is a mirror image of Figure 8.1.1.1.

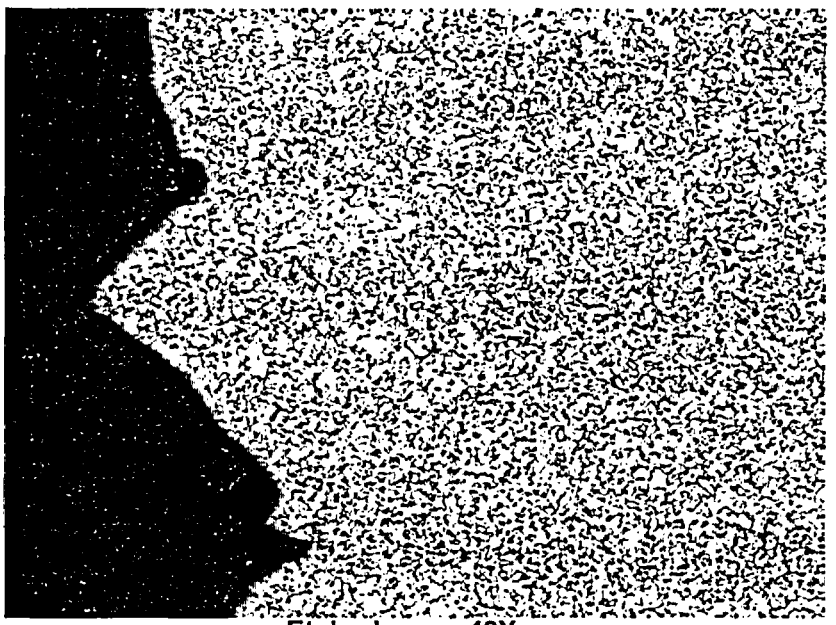

Etched 48X

Figure 8.1.1.3: Higher magnification micrograph, which indicates a slightly faster local corrosion rate along the striations.

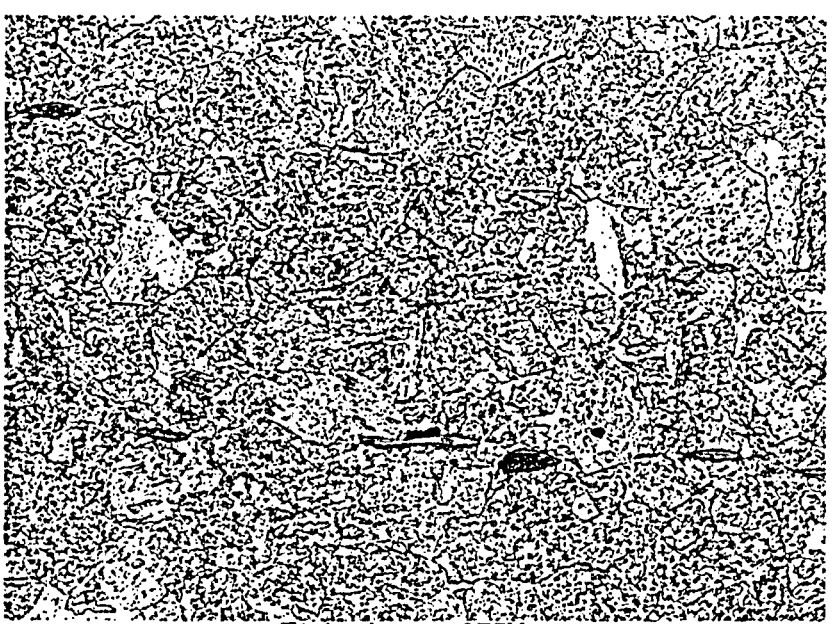

Etched 375X

Figure 8.1.1.4: Micrograph showing the typical tempered martensitic microstructure of SA-533, Gr. B (mod), Cl. 1 low alloy steel plate.

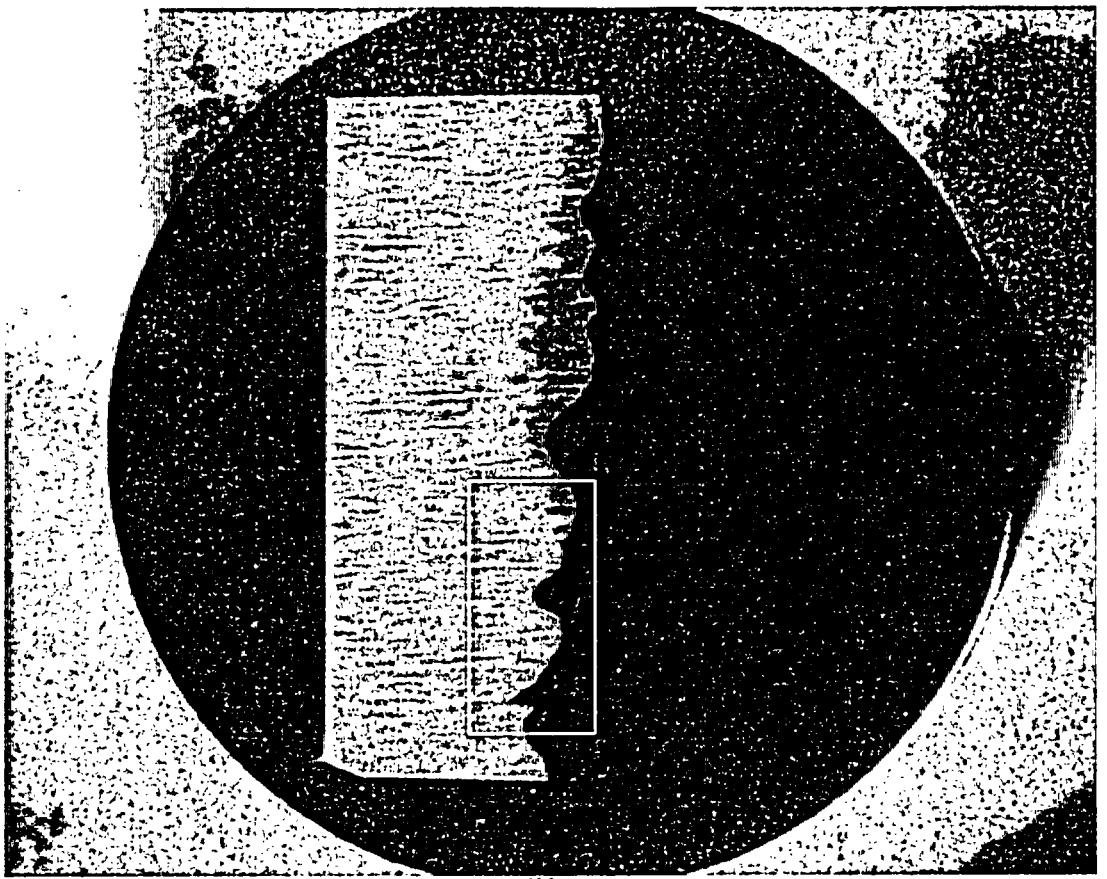

Figure 8.1.2.1: Macro photograph of metallurgical mount A1B4. Refer to Figures 5.13 and 5.14 for the sample location. The white box indicates the area shown at higher magnification in Figure 8.1.2.2.

Figure 8.1.2.2: Higher magnification micrograph showing the horizontal striations aligned with the major axis of the RV head low alloy steel plate (SA-533, Gr. B (mod), Cl. 1). However, unlike Figure 8.1.1.3, the striations do not appear to promote a faster corrosion rate locally.

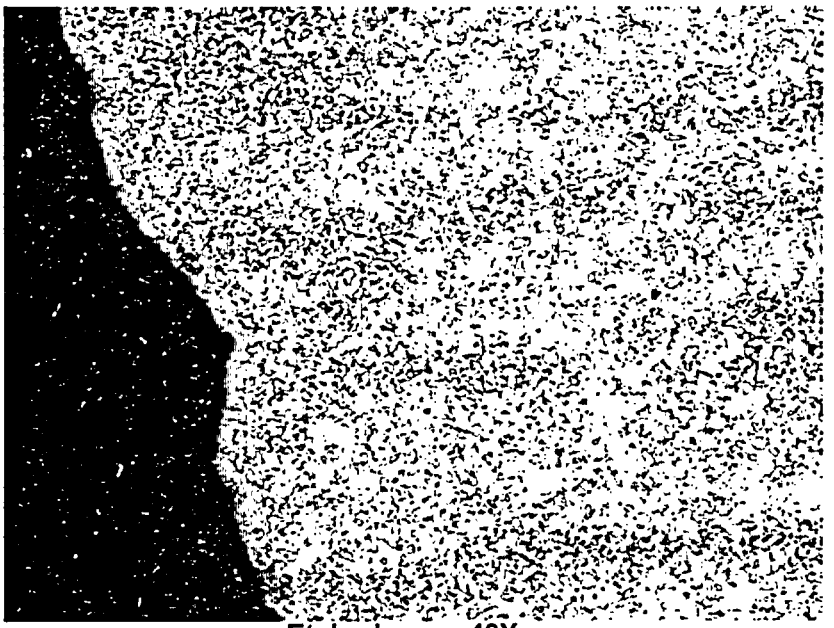

Figure 8.1.2.3: At higher magnification, the local corrosion rate along the striations is increased only very slightly.

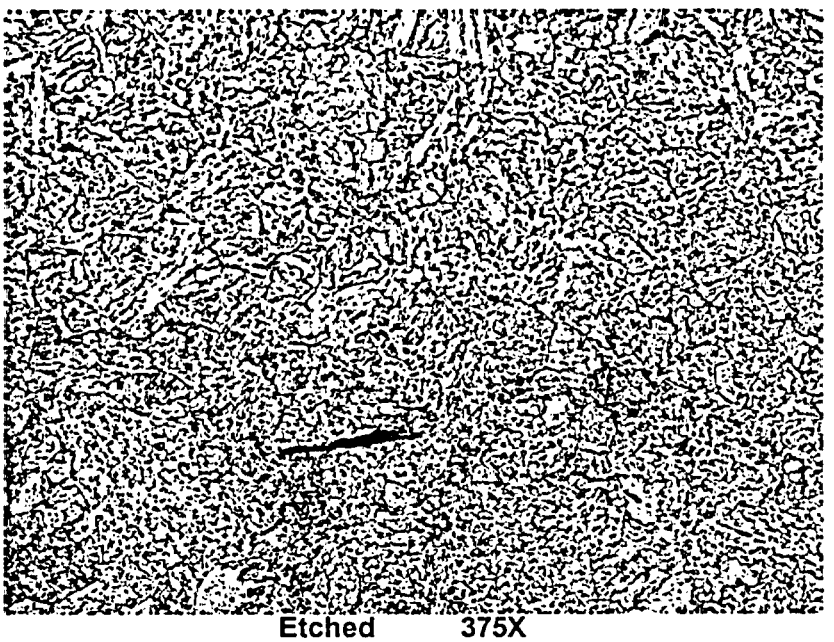

Figure 8.1.2.4: Micrograph showing the typical tempered martensitic microstructure of SA-533, Gr. B (mod), Cl. 1 low alloy steel plate.

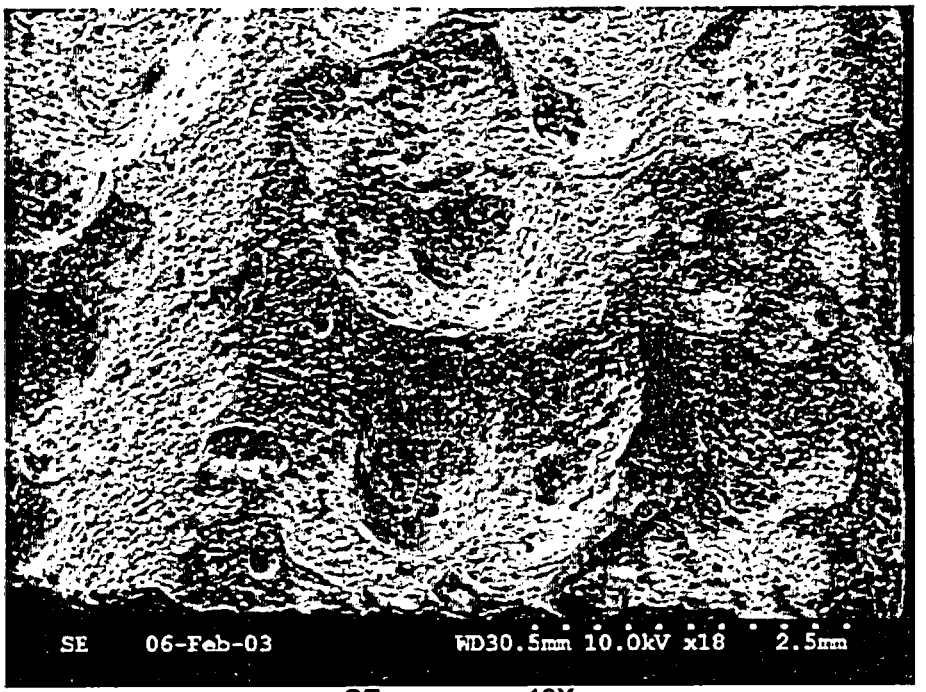

SE 18X

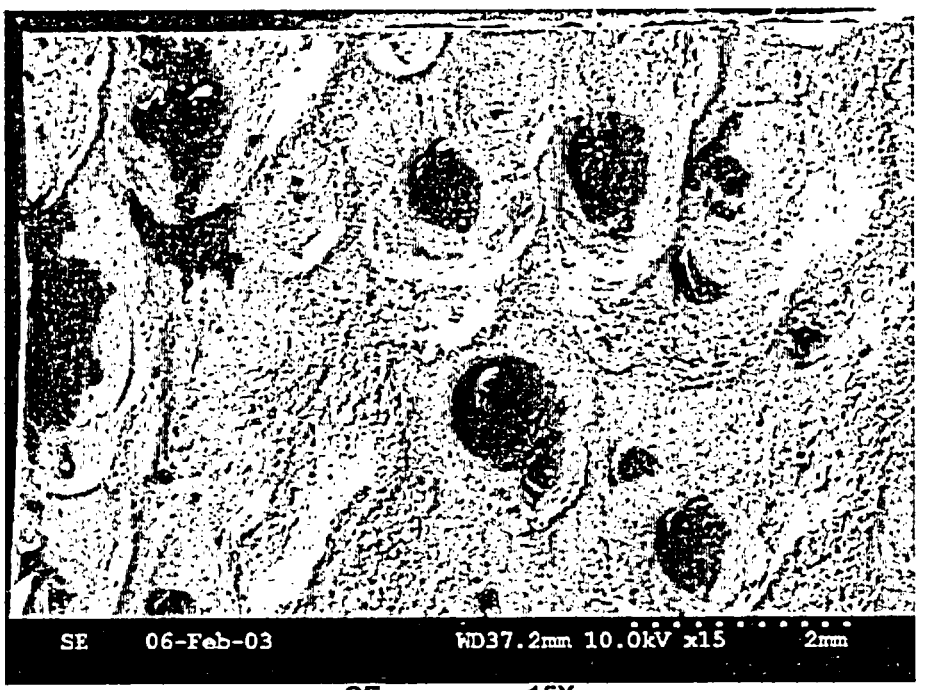

SE 15X

Figure 8.1.3.1: Low magnification SE micrographs of cavity wall surface near 90°. The surface contains generally round depressions measuring ~0.039" or less in diameter.

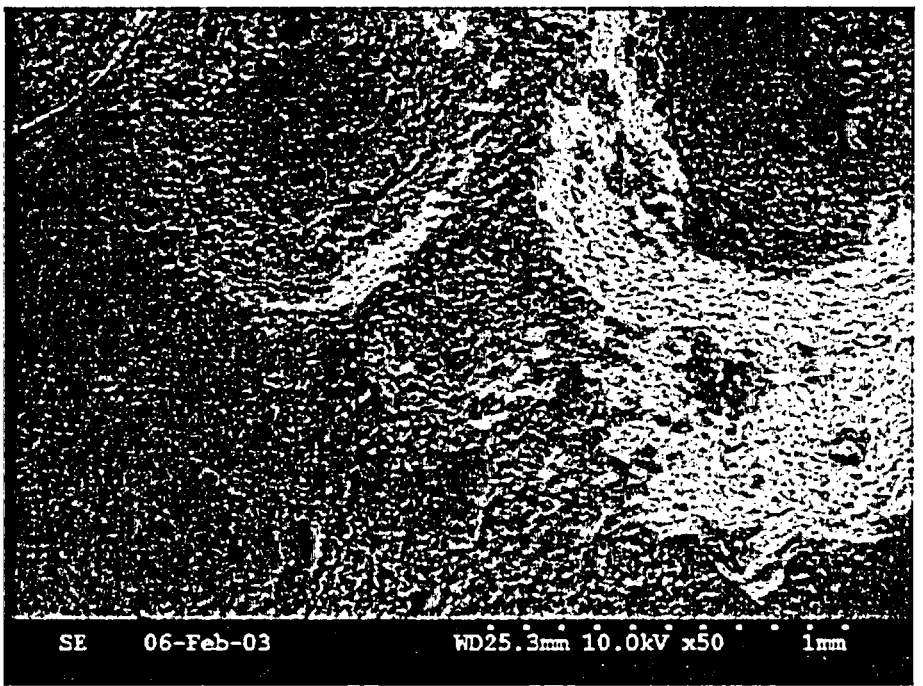

SE 50X

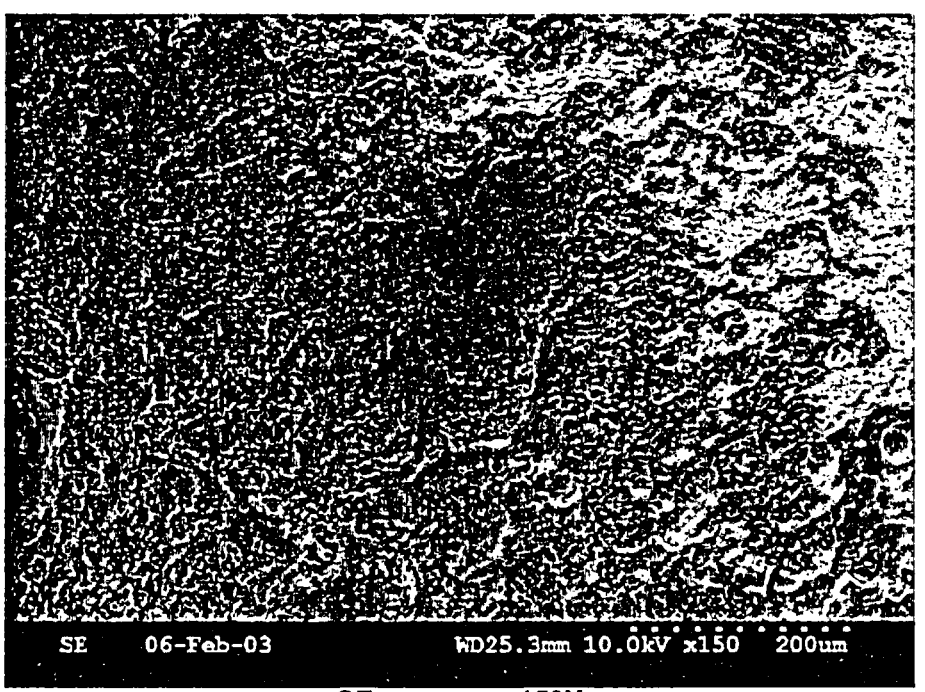

SE 150X

Figure 8.1.3.2: Higher magnification micrographs of the cavity side wall near 90°.

SE 100X

SE 1,000X

Figure 8.1.3.3: SE micrographs showing corrosion products on cavity side wall near 90°.

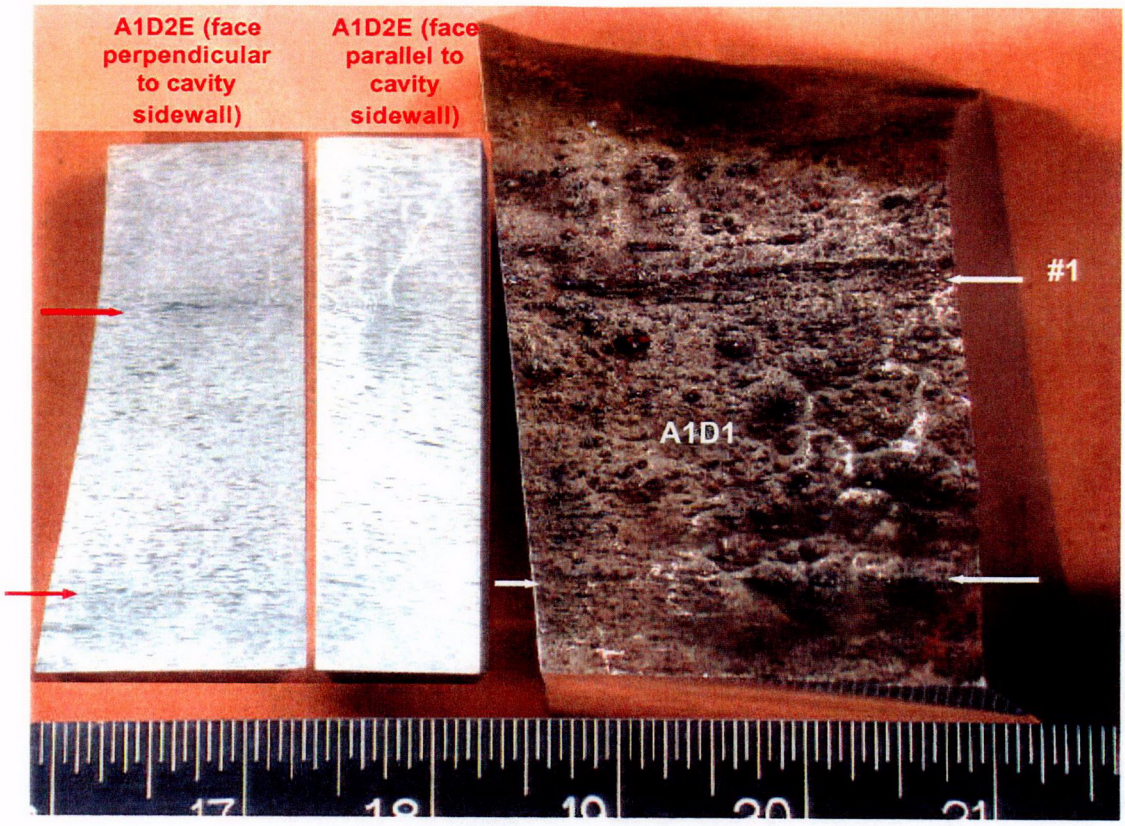

Figure 8.2.1.1: Low magnification photographs showing macro etch results. Arrows indicate corrosion grooves associated with corresponding micro-structural banding. Macro etch was performed on two surfaces of sample A1D2E ground with 400 grit paper. Etchant: 10% nital.

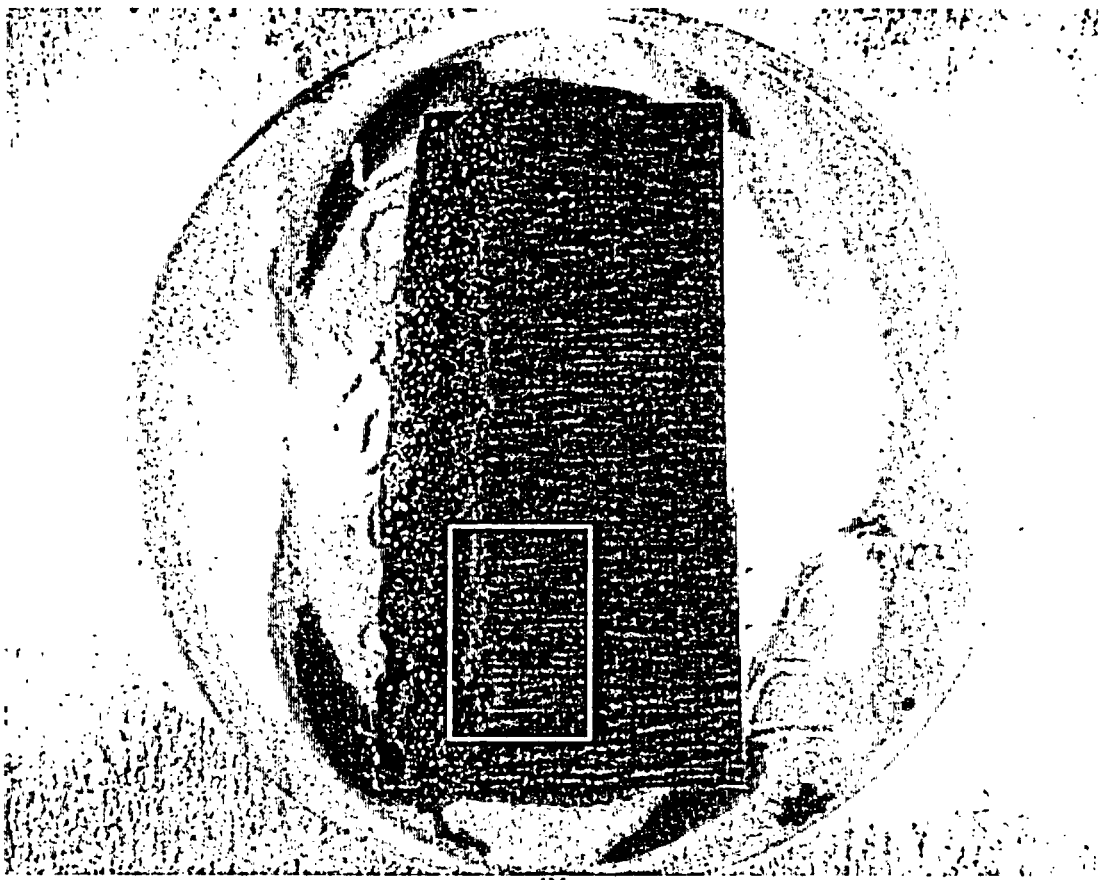

Figure 8.2.2.1: Macro photograph of metallurgical mount A1D2B1. Refer to Figures 5.13, 5.15, and 5.16 for the sample location. The white box indicates the area shown at higher magnification in Figure 8.2.2.2.

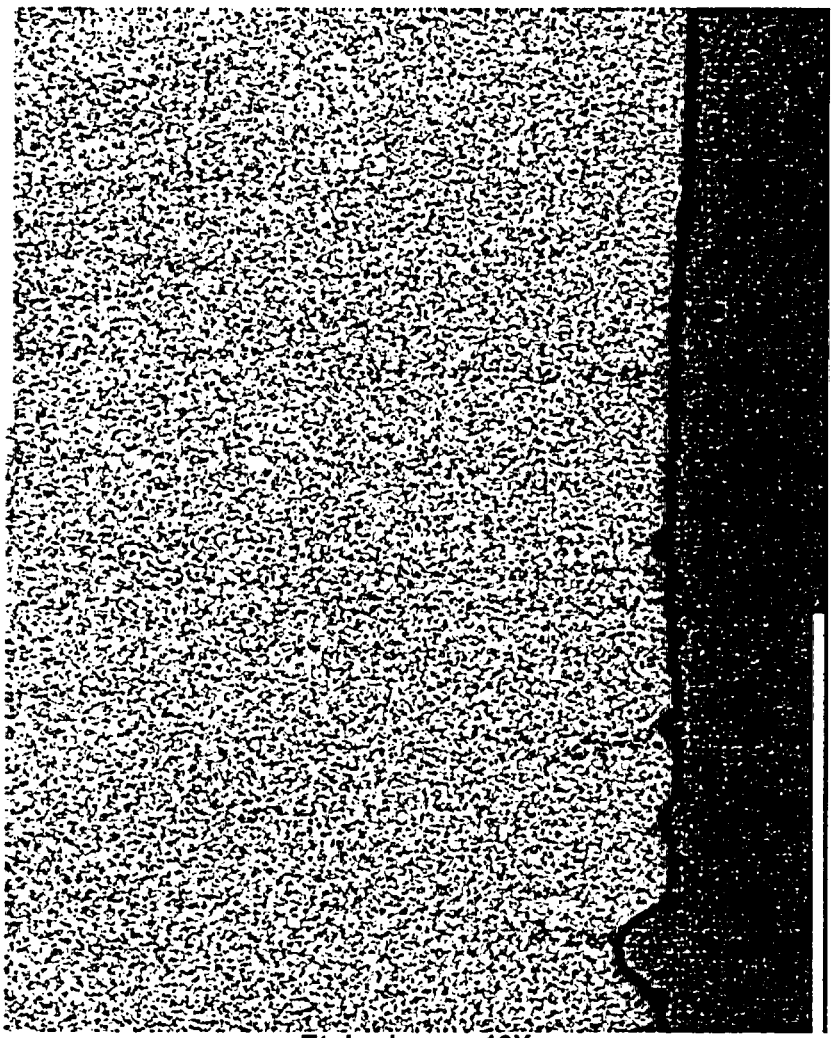

Figure 8.2.2.2: Slightly higher magnification micrograph showing the horizontal striations aligned with the major axis of the RV head low alloy steel plate (SA-533, Gr. B (mod), Cl. 1). Striations appear to be caused by a very slightly faster local corrosion rate. Note that this micrograph is a mirror image of Figure 8.2.2.1.

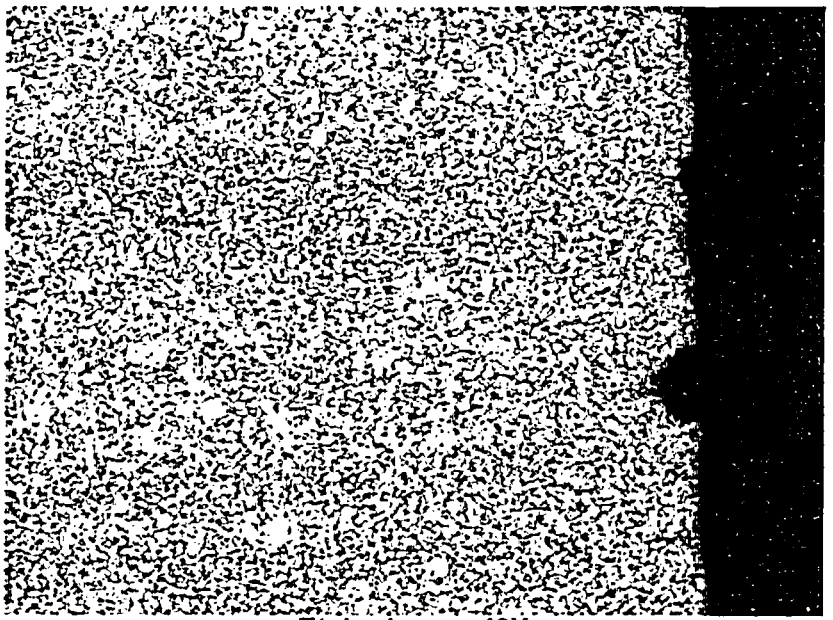

Etched 48X

Figure 8.2.2.3: Higher magnification detail of Figure 8.2.2.2, which suggests a slightly faster local corrosion rate along the striations.

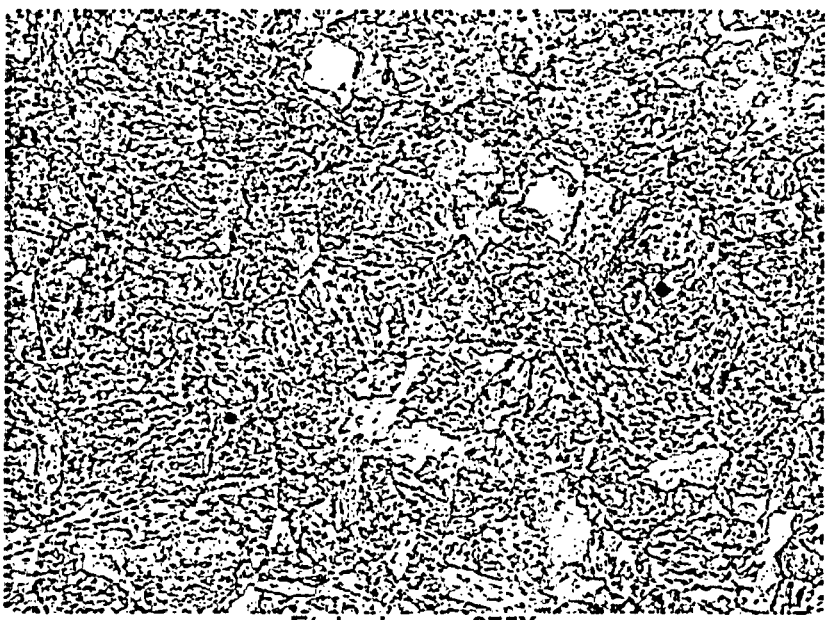

Etched 375X

Figure 8.2.2.4: Micrograph showing the typical tempered martensitic microstructure of SA-533, Gr. B (mod), Cl. 1 low alloy steel plate.

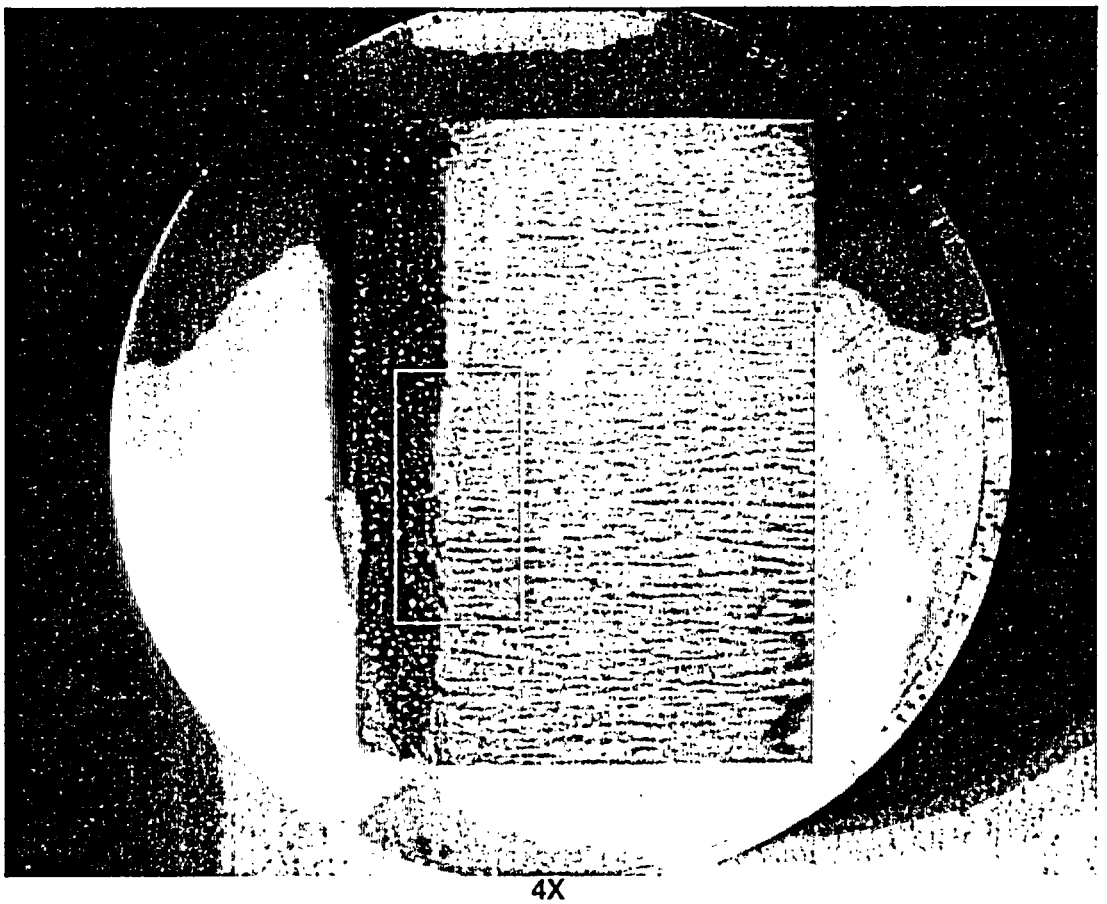

Figure 8.2.3.1: Macro photograph of metallurgical mount A1D2D1. Refer to Figures 5.13, 5.15, and 5.16 for the sample location. The white box indicates the area shown at higher magnification in Figure 8.2.3.2.

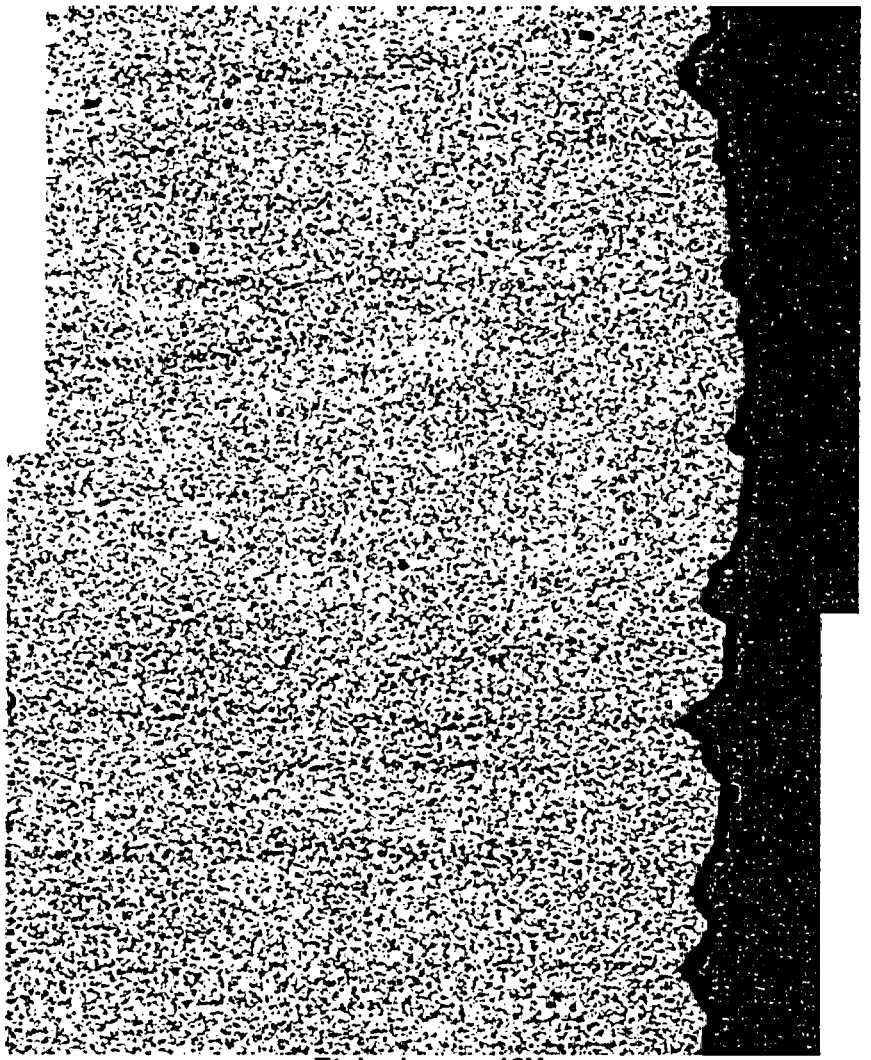

Figure 8.2.3.2: Higher magnification detail of Figure 8.2.3.1 showing the horizontal striations aligned with the major axis of the RV head low alloy steel plate (SA-533, Gr. B (mod), Cl. 1). Striations appear to be caused by a very slightly faster local corrosion rate.

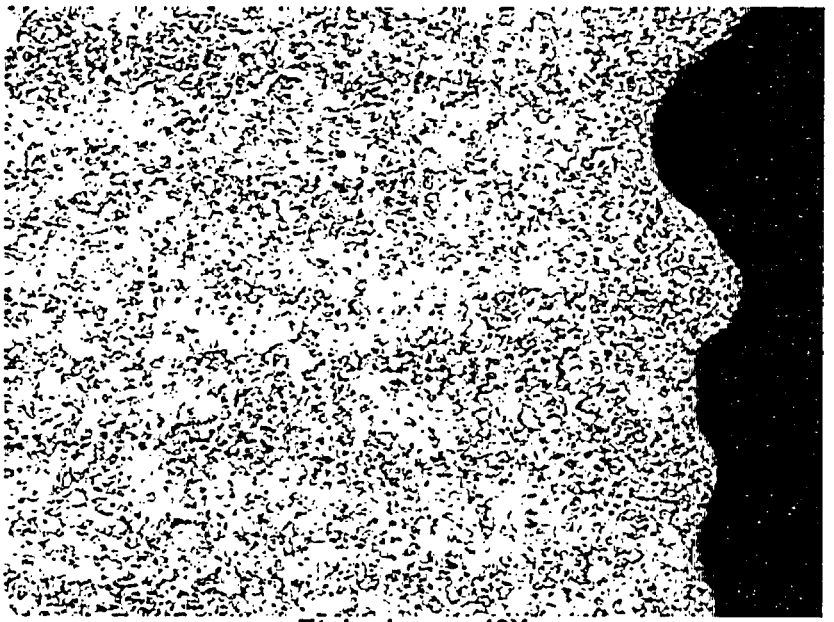

Etched 48X

Figure 8.2.3.3: Higher magnification detail of Figure 8.2.3.2, which suggests a slightly faster local corrosion rate along the striations.

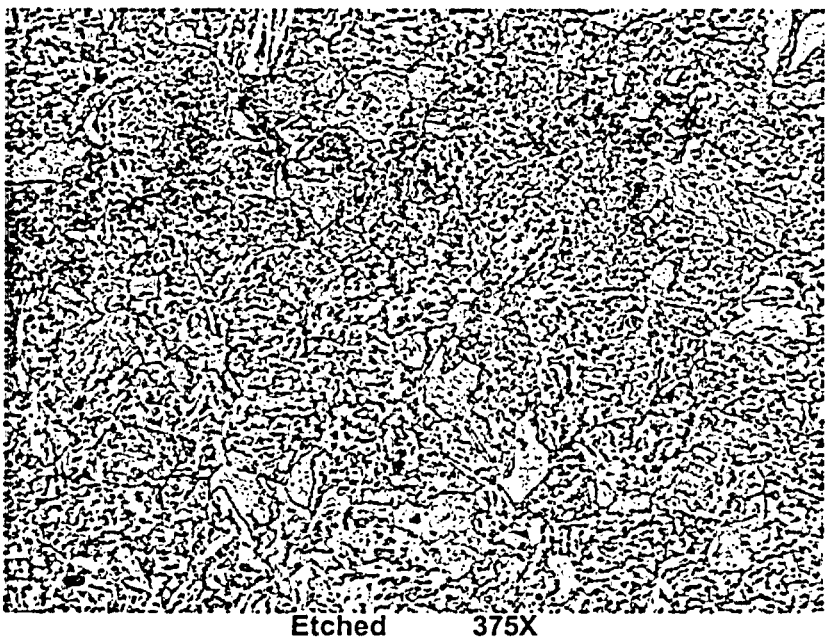

Etched 375X

Figure 8.2.3.4: Micrograph showing typical tempered martensitic microstructure of SA-533, Gr. B (mod), Cl. 1 low alloy steel plate.

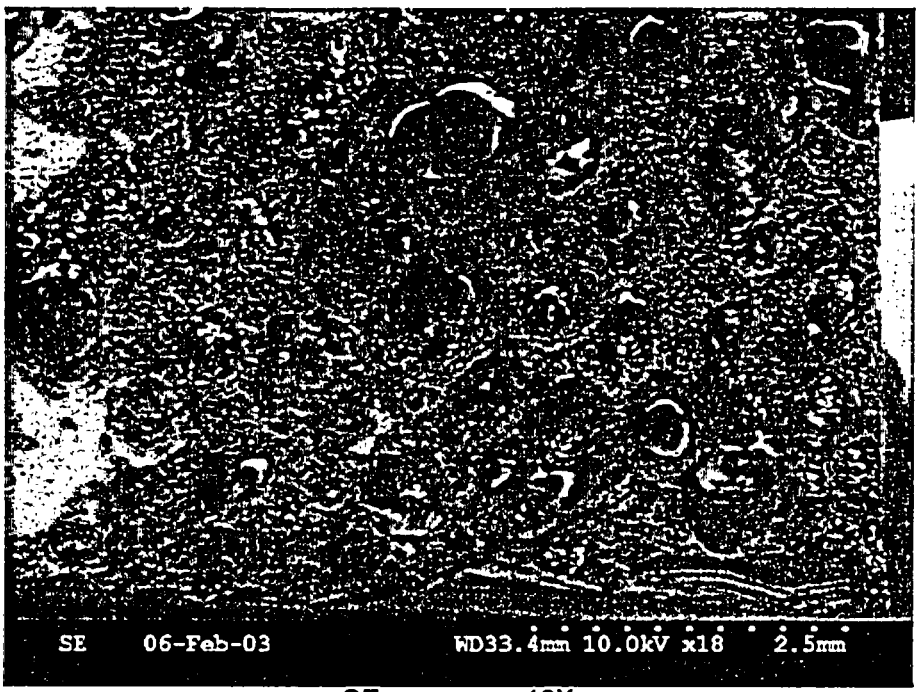

SE 18X

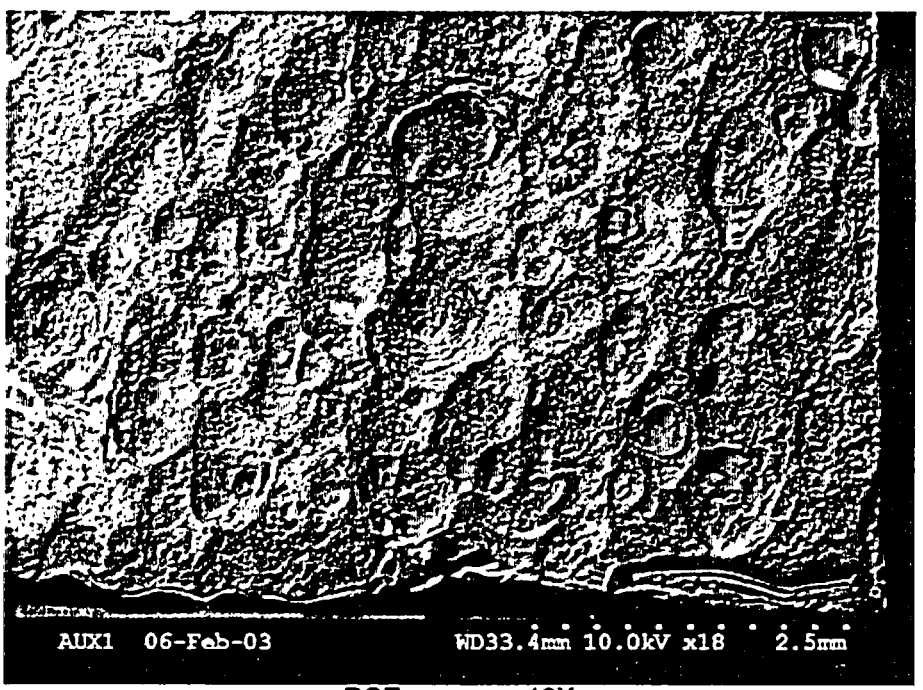

BSE 18X

Figure 8.2.4.1: SE (top) and BSE (bottom) micrographs of the cavity wall surface near 270°. The surface contained rounded depressions measuring 0.020" in diameter or less. Orientation of micrographs: lower portion of cavity to the right and upper portion to the right. Nozzle #3 is closer to lower edge of micrograph.

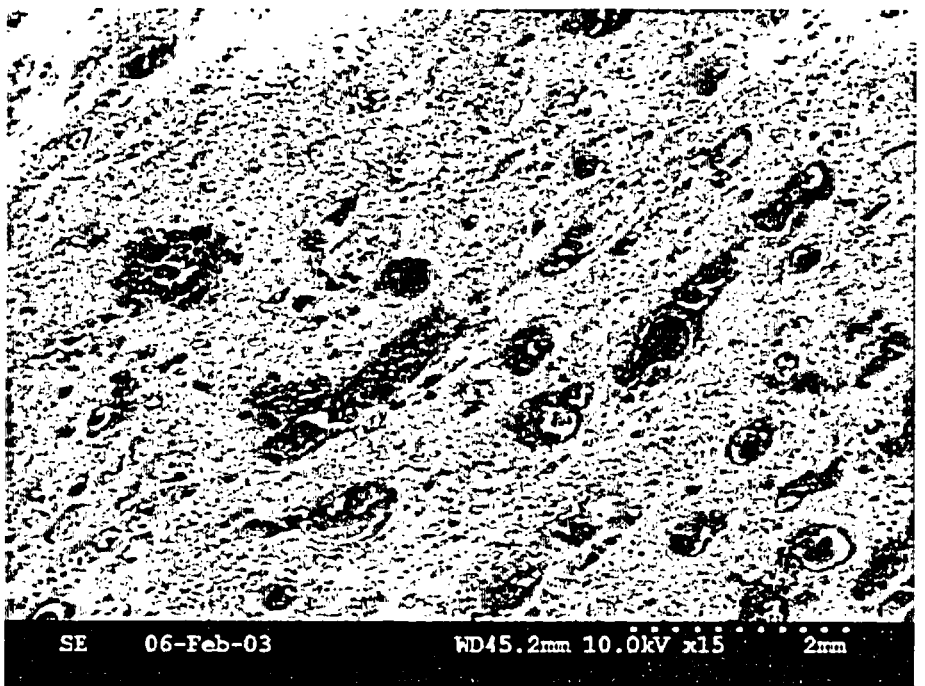

SE 15X

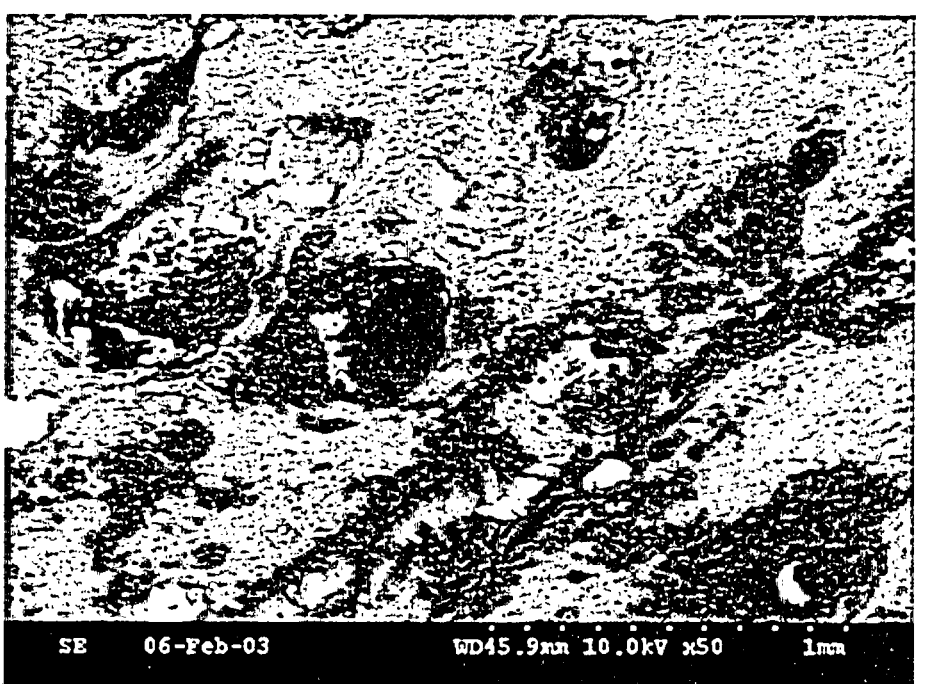

SE 50X

Figure 8.2.4.2: SE micrographs of cavity side wall near 270°. These micrographs suggest that larger (~1 mm dia.) shallower depressions are caused by acid boiling and smaller (~0.3 mm dia.) deeper depressions are caused by inclusions.

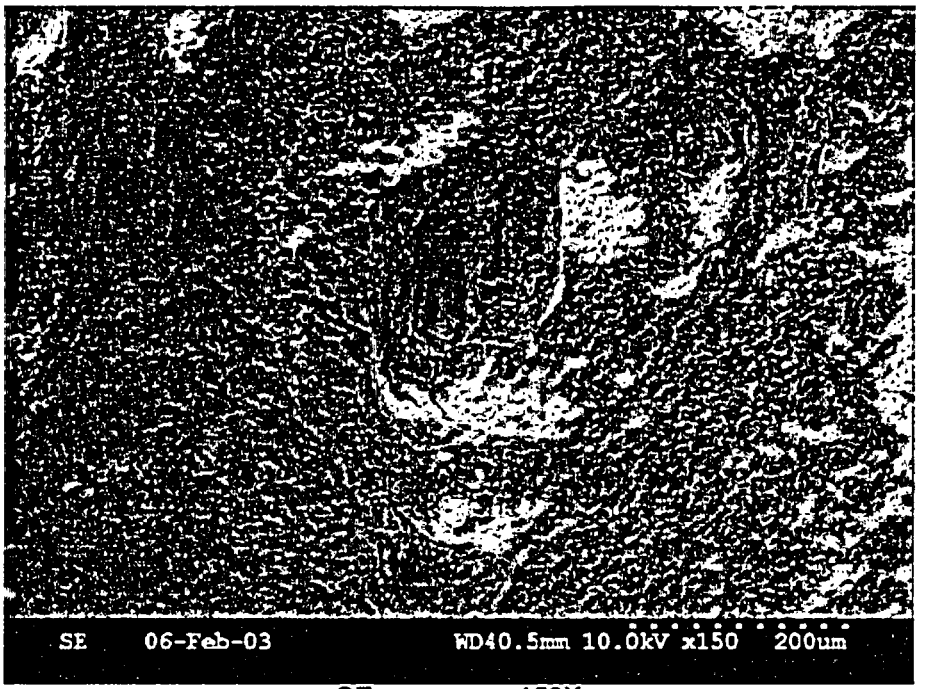

SE 150X

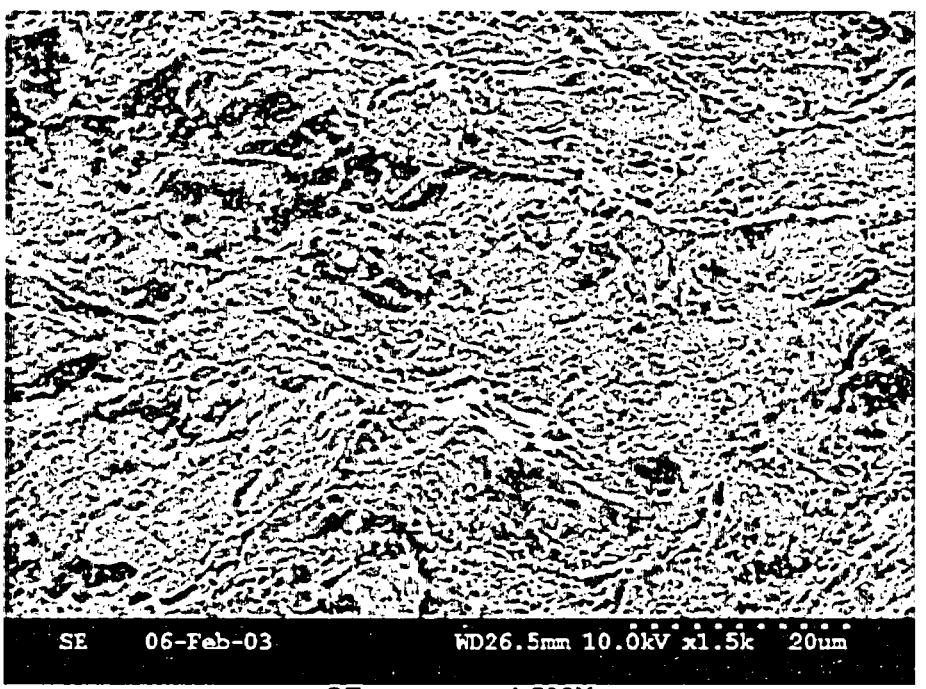

SE 1,500X

Figure 8.2.4.3: Higher magnification SE micrograph showing corrosion products on cavity side wall near 270°.

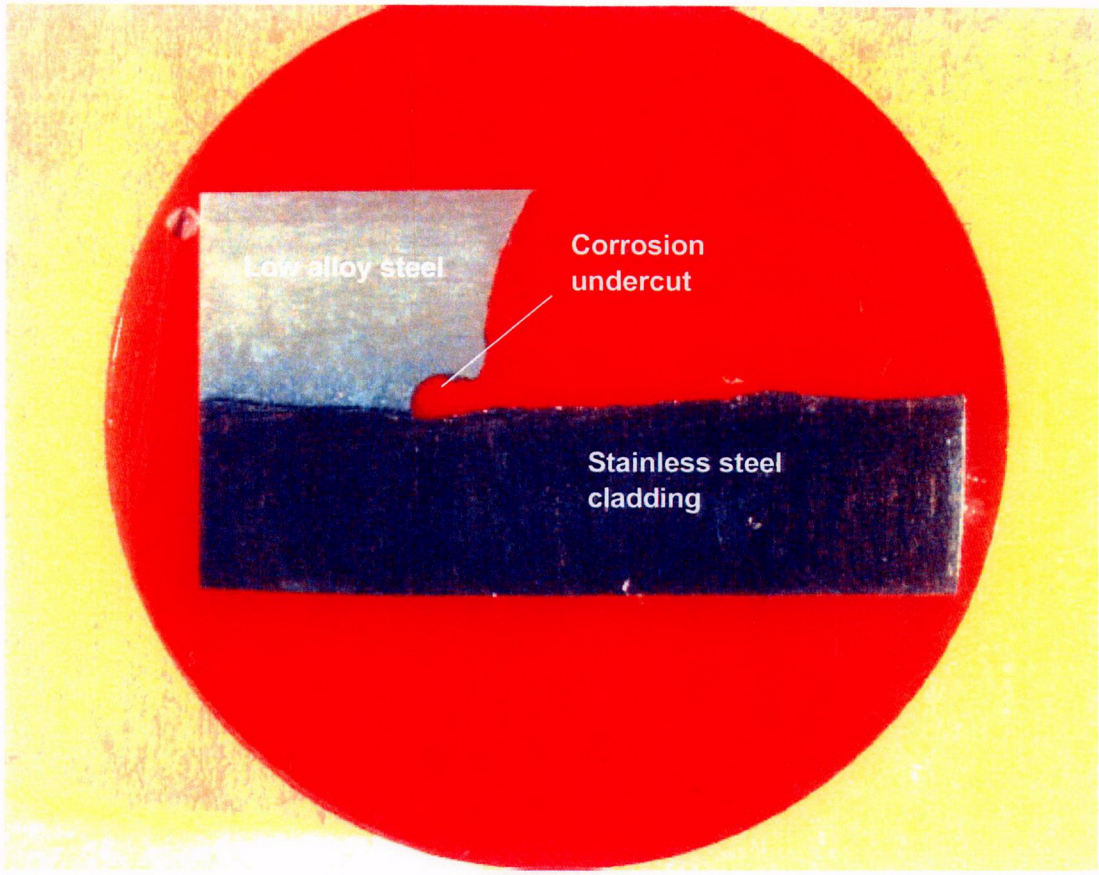

Figure 8.3.1.1: Macro photograph of metallographic mount A2A7D. Refer to Figures 5.1 and 5.11 for the sample location.

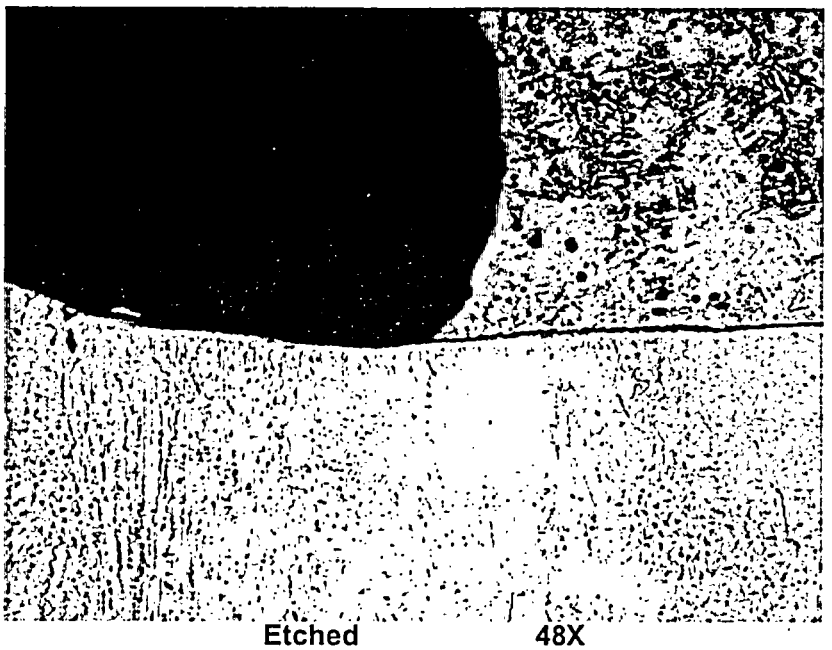

Figure 8.3.1.2: Micrograph showing the edge of the exposed cladding in the undercut region. Note: the micrograph is a mirror image of the macrograph in Figure 8.3.1.1.

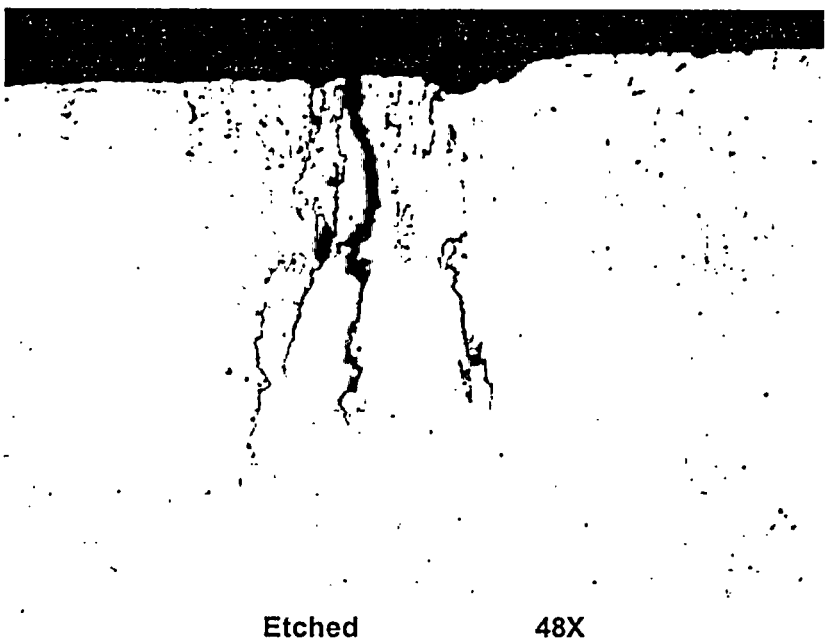

Figure 8.3.1.3: Micrograph showing intergranular attack (IGA) and intergranular or interdendritic cracking in the cladding. The maximum depth of the crack tip is approximately 0.047" below the exposed cladding surface.

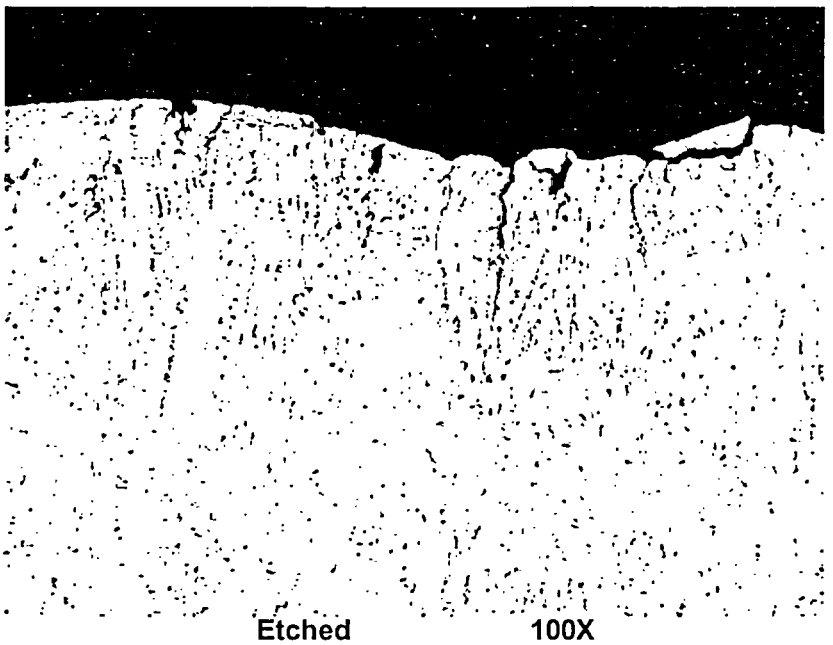

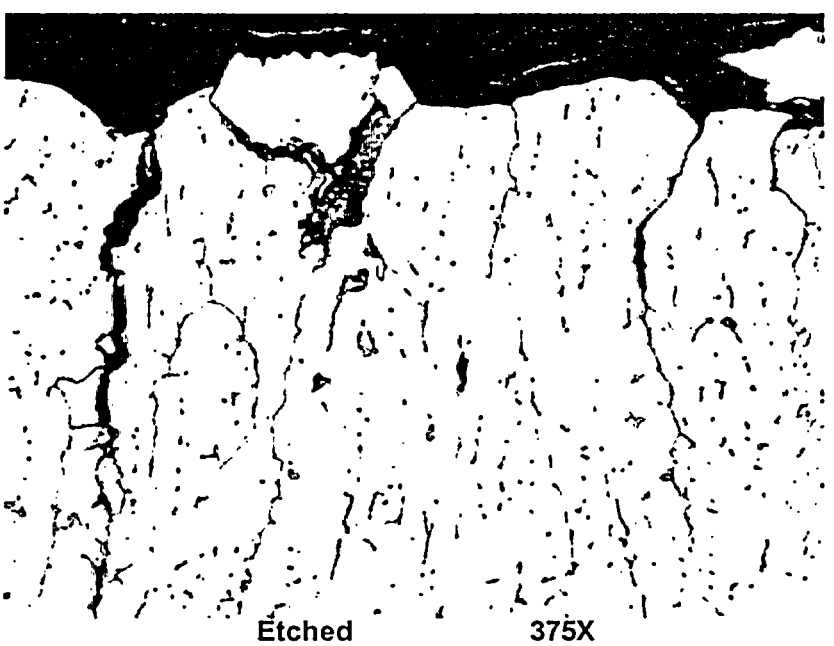

Figure 8.3.1.4: Micrographs showing intergranular attack (IGA) and intergranular or interdendritic cracking on the exposed cladding surface.

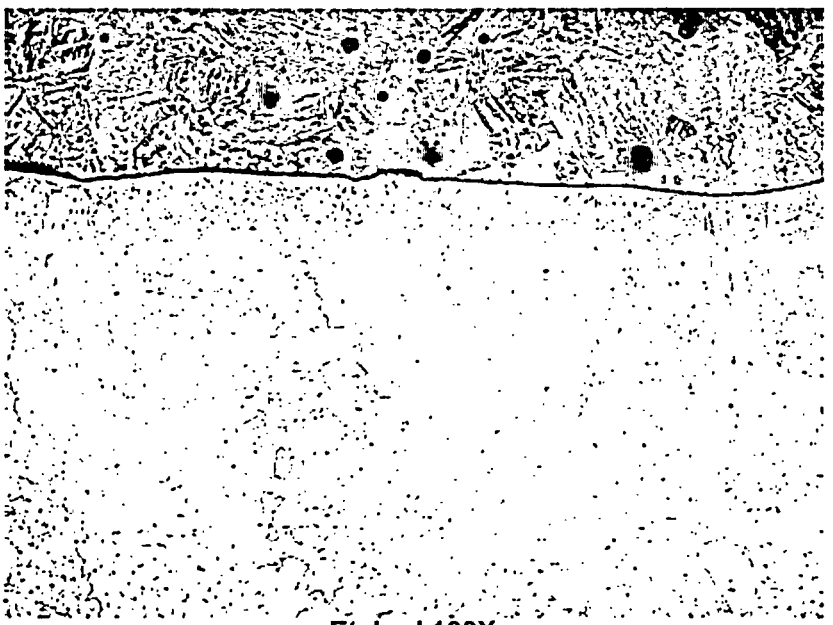

Etched 100X

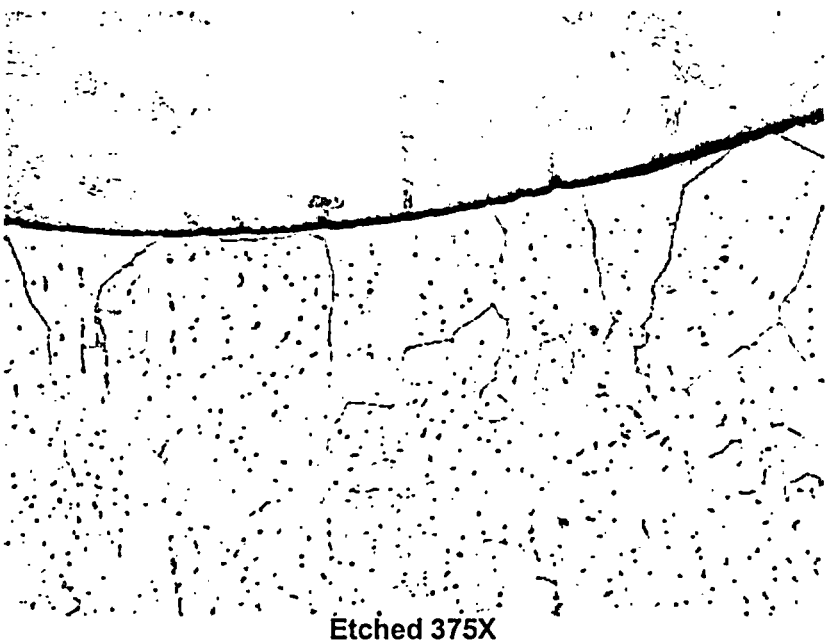

Etched 375X

Figure 8.3.1.5: Micrographs showing the interface between the low alloy steel (above the fusion line) and the stainless steel cladding (below the fusion line).

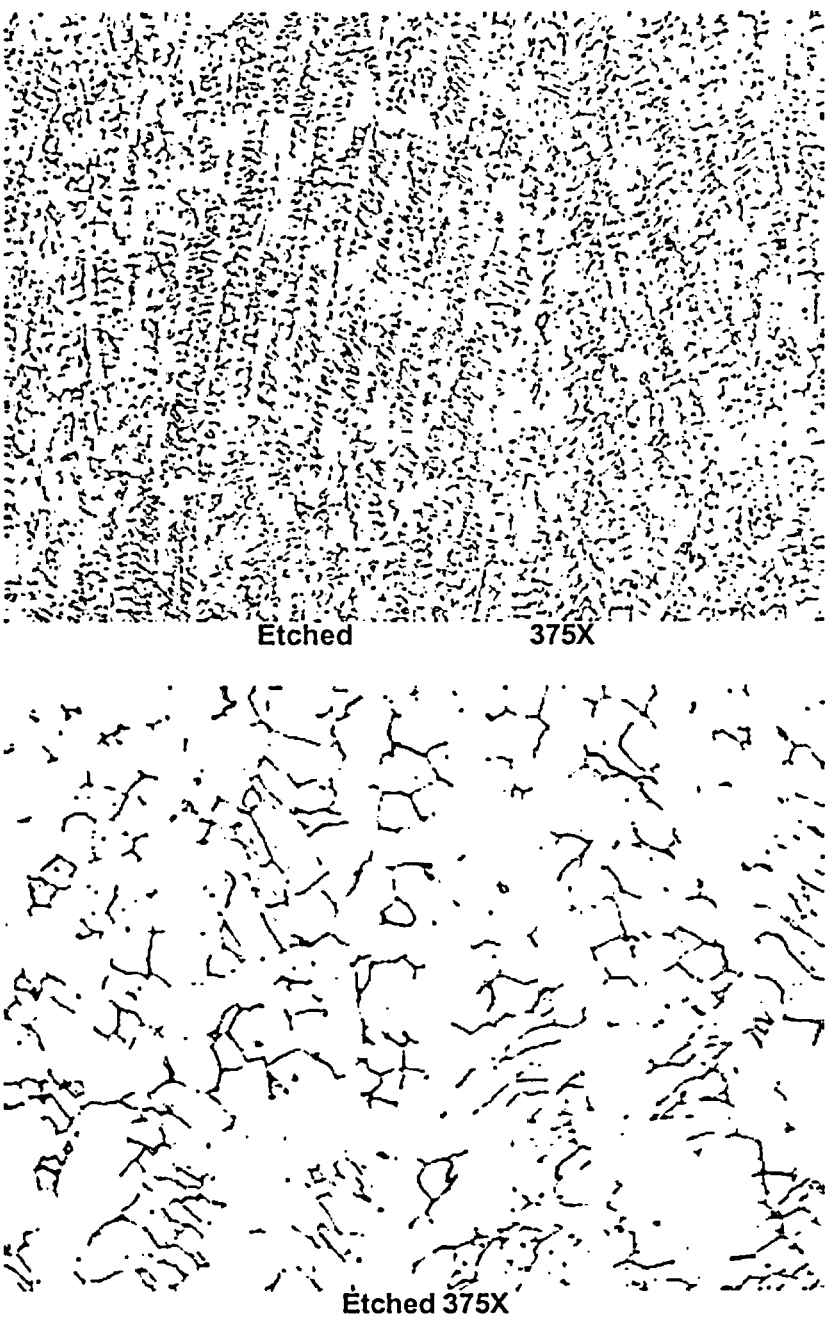

Figure 8.3.1.6: Micrographs showing typical stainless steel cladding microstructure. The interdendritic solidification structure is delineated by small pools (or islands) of ferrite in an austenitic matrix.

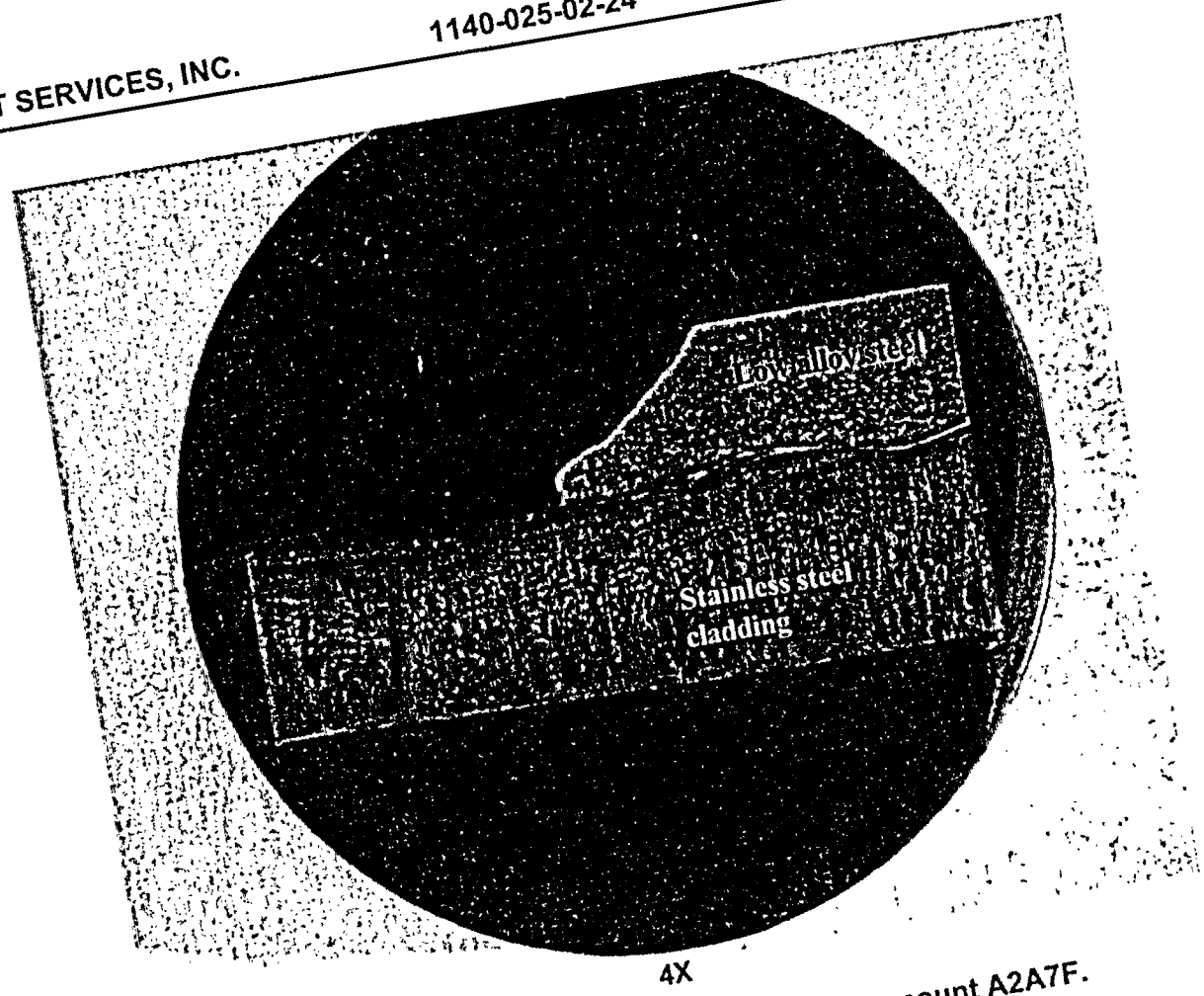

4X

Figure 8.3.2.1: Macro photograph of metallographic mount A2A7F.
Refer to Figures 5.1 and 5.11 for the sample location.

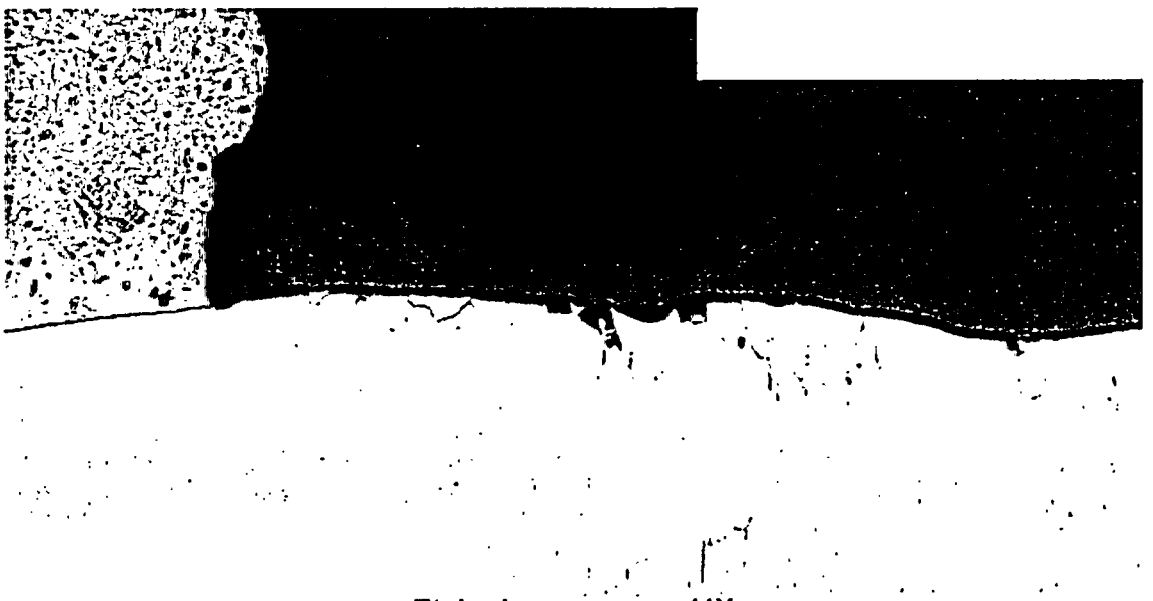

Etched 41X

Figure 8.3.2.2: Micrograph showing the exposed cladding surface. A slight undercut is evident in the low alloy steel. Note: the micrograph is a mirror image of the macrograph in Figure 8.3.2.1.

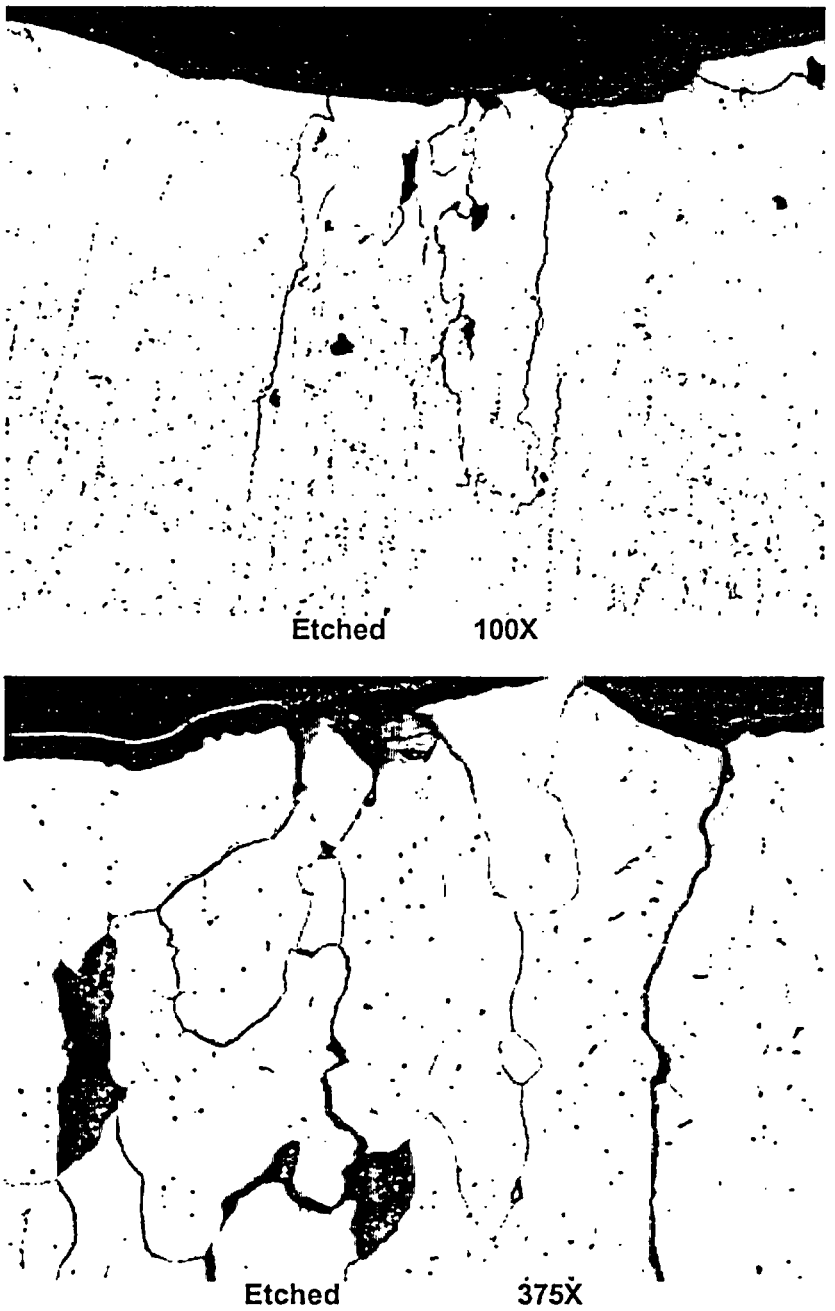

Figure 8.3.2.3: Micrographs showing intergranular attack (IGA) and intergranular or interdendritic cracking. The maximum depth of the crack tip is approximately 0.024" below the exposed cladding surface.

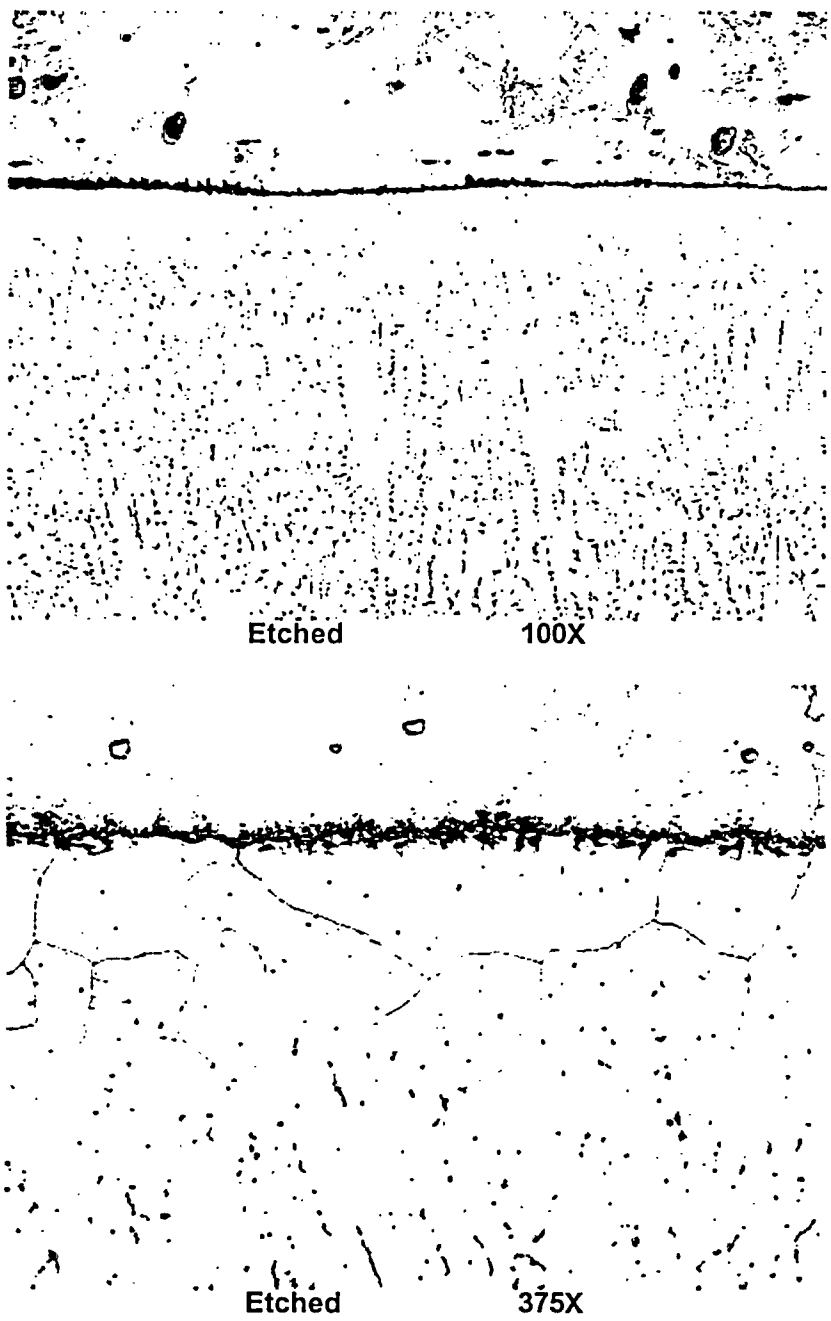

Figure 8.3.2.4: Micrographs showing the interface between the low alloy steel (above the fusion line) and the stainless steel cladding (below the fusion line).

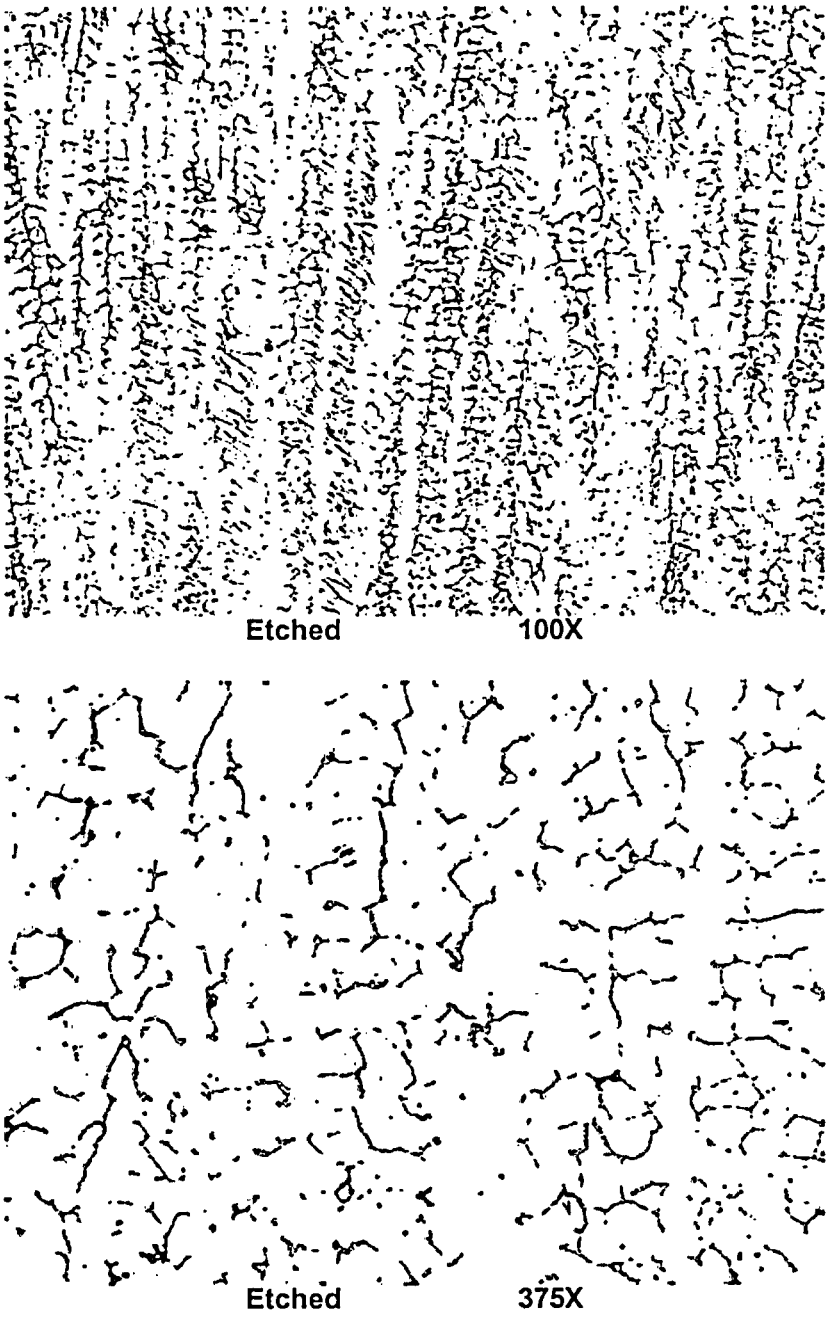

Figure 8.3.2.5: Micrographs showing the typical stainless steel cladding microstructure. The interdendritic solidification structure is delineated by small pools (or islands) of ferrite in an austenitic matrix.

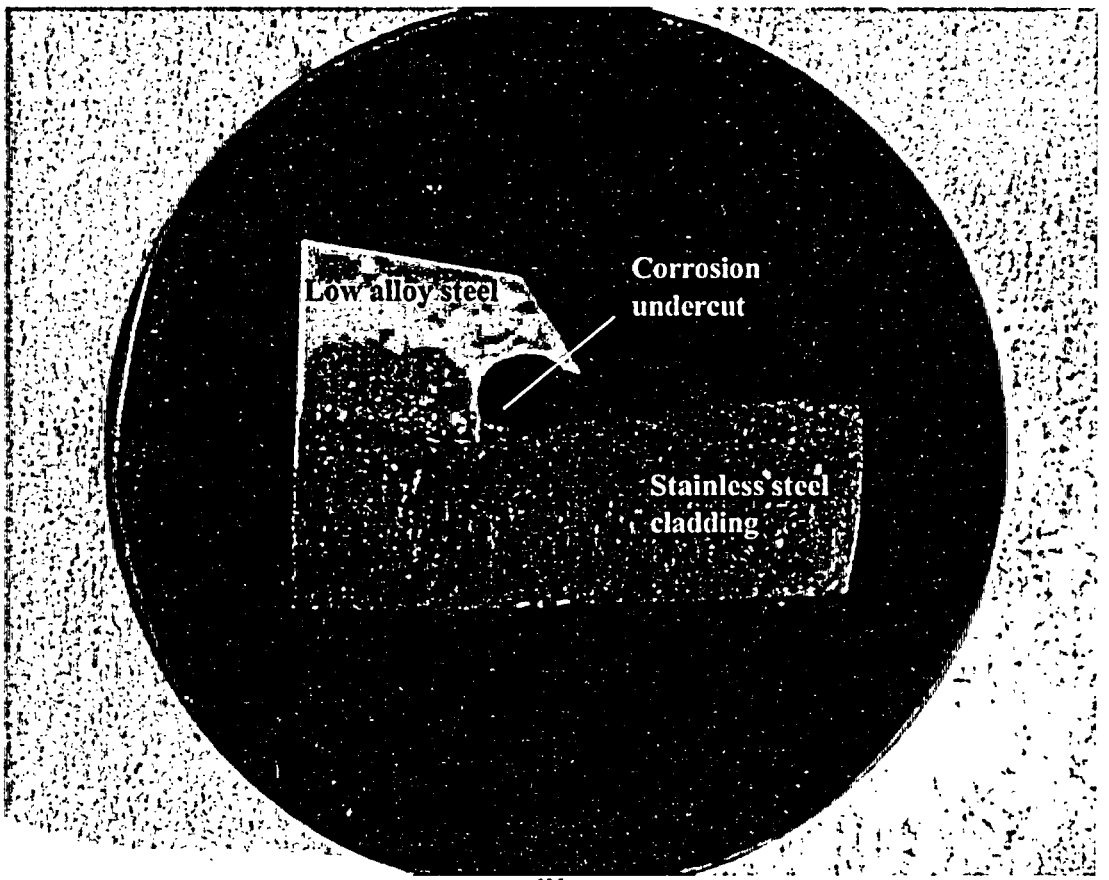

Figure 8.3.3.1: Macro photograph of metallographic mount A2A7K. Refer to Figures 5.1 and 5.11 for the sample location.

Etched 48X

Figure 8.3.3.2: Micrograph showing the edge of the exposed cladding in the undercut region. Note: the micrograph is a mirror image of the macrograph in Figure 8.3.3.1.

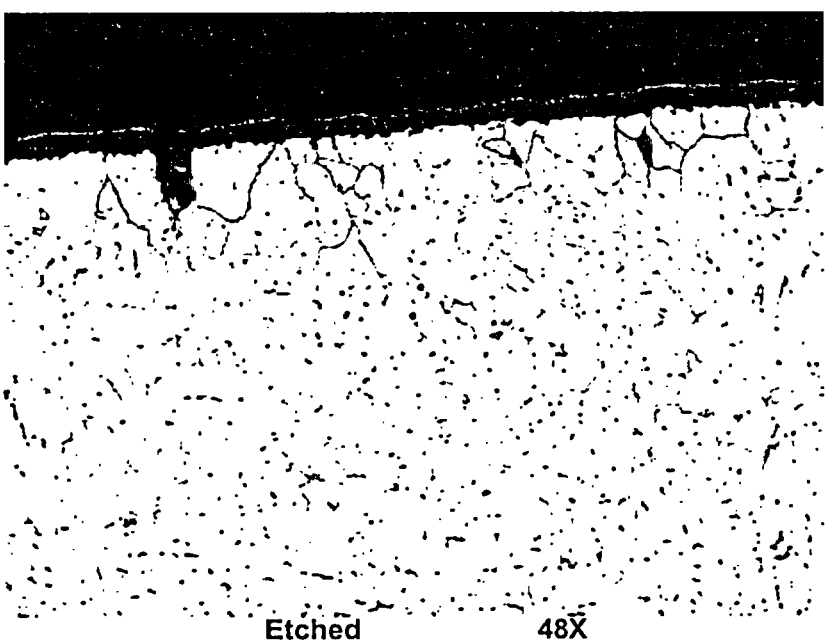

Etched 48X

Figure 8.3.3.3: Micrograph showing minor intergranular attack (IGA) in the exposed cladding surface.

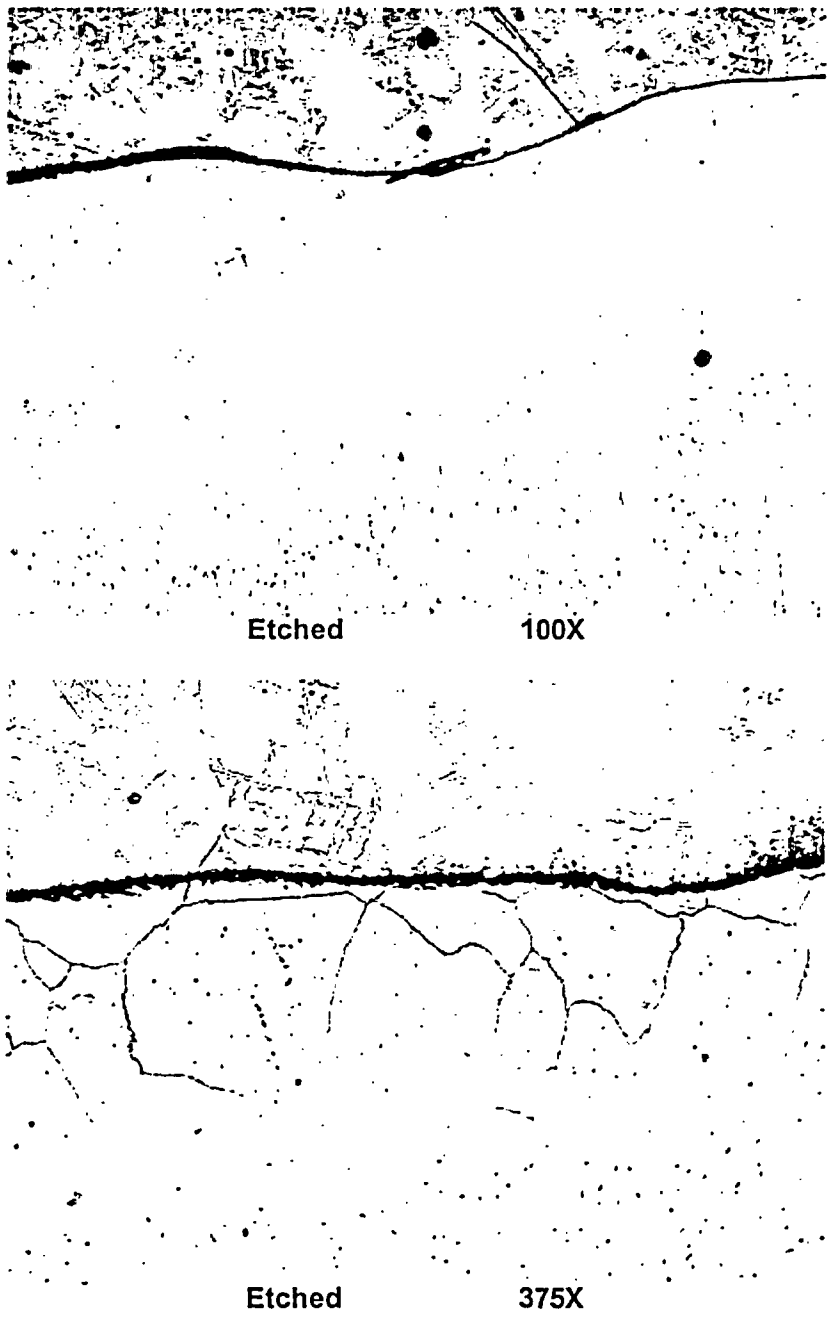

Figure 8.3.3.4: Micrographs showing the interface between the low alloy steel (above the fusion line) and the stainless steel cladding (below the fusion line).

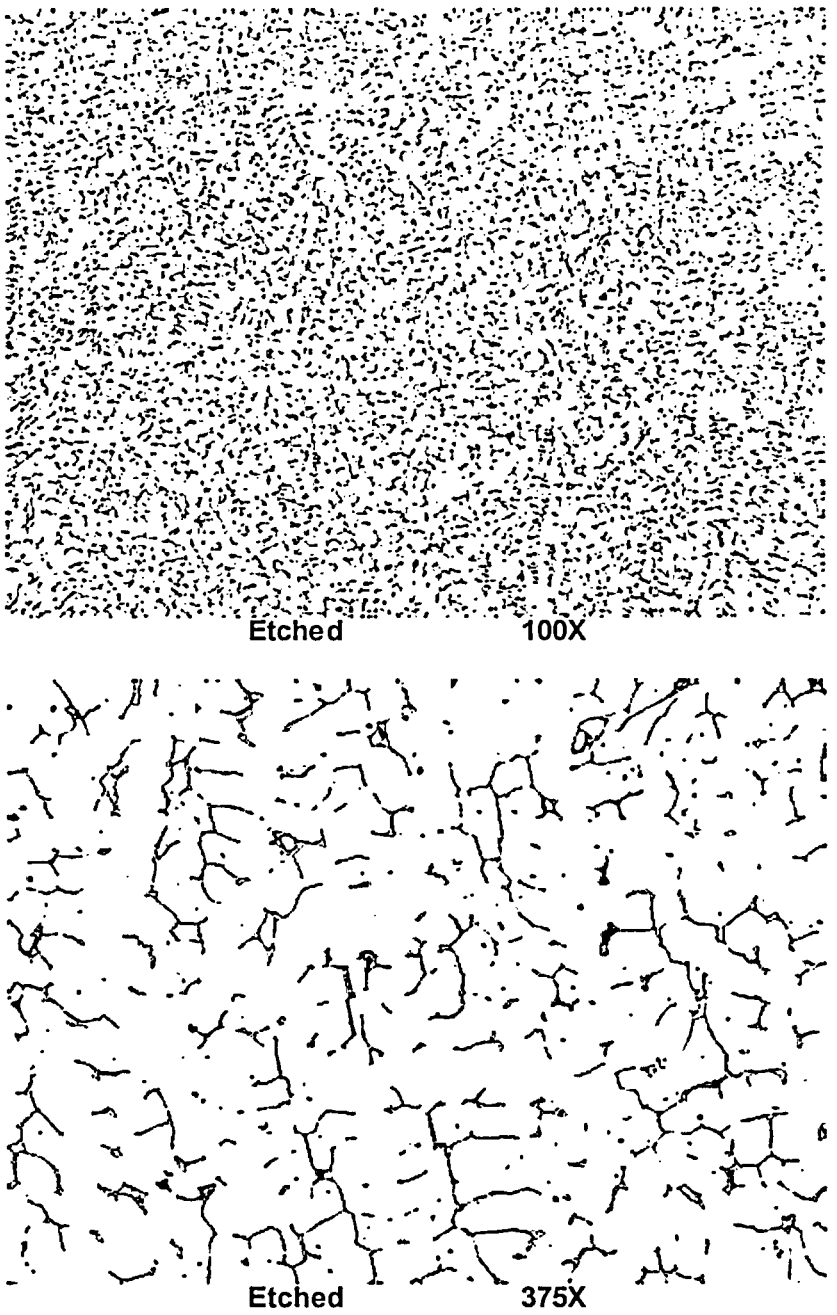

Figure 8.3.3.5: Micrographs showing the typical stainless steel cladding microstructure. The interdendritic solidification structure is delineated by small pools (or islands) of ferrite in an austenitic matrix.